

RESEARCH ARTICLE SUMMARY

NEUROSCIENCE

Compartmentalized dendritic plasticity during associative learning

Simon d'Aquin, Andras Szonyi, Mathias Mahn, Sabine Krabbe, Jan Gründemann, Andreas Lüthi*

INTRODUCTION: Learning is mediated by experience-dependent plasticity of neuronal function. Although we have a detailed knowledge of synaptic and dendritic plasticity in vitro, learning-induced functional changes in vivo are mostly assessed by use of soma-centric methods such as unit recordings or imaging of somatic Ca^{2+} activity. However, these methods do not reveal the complexity of dendritic signaling and its regulation by local neuronal circuitry. Moreover, because dendrites are functionally independent subcellular compartments that dynamically integrate incoming information and thereby affect a neuron's input-output function, the questions arise whether compartmentalized plasticity occurs during learning and which mechanisms ultimately control somatic output in behaving animals.

RATIONALE: To investigate dendritic function and plasticity in vivo, we focused on the lateral amygdala (LA), a subcortical brain structure that is central to classical auditory fear conditioning, a fast and robust form of associative learning. During auditory fear conditioning, an auditory conditioned stimulus (CS; typically a pure tone or white noise) is paired with an aversive unconditioned stimulus (US; typically a foot shock), which results in the induction of Hebbian activity-dependent synaptic potentiation at auditory synaptic inputs onto LA principal neurons (PNs). This view has recently been extended by studies reporting that similar proportions of neurons up- and down-

regulate their CS response upon fear conditioning, suggesting that fear learning involves more diverse forms of plasticity. However, these studies relied on measurements of somatic activity, whereas dendritic activity and plasticity during associative learning was not explored.

RESULTS: To image the activity of dendrites and somas of amygdala PNs deep in the brain of awake mice undergoing classical fear conditioning, we used gradient-index lens-based high-resolution two-photon microscopy across multiple days. We show that sensory stimulation induces compartmentalized dendritic responses controlled by dendrite-targeting somatostatin-expressing (SST+) interneurons. Spontaneous inputs to PN dendrites are suppressed by SST+ interneurons, whereas salient sensory stimuli transiently alleviate SST+ interneuron-mediated inhibition of PN dendrites likely through VIP+ interneurons. In most cases, this evokes highly correlated somatic and dendritic sensory responses. However, sensory input can also lead to isolated dendritic responses without concomitant somatic output, indicating that dendrites of LA PNs can integrate auditory inputs locally.

The relief of SST+ interneuron-mediated dendritic inhibition is necessary to amplify dendritic CS responses during conditioning, which is consistent with the notion that disinhibition through SST+ interneurons opens a temporal window during which CS inputs are eligible for the induction of associative den-

dritic plasticity upon concomitant exposure to an aversive US.

Fear conditioning induces bidirectional plasticity of somatic CS responses that correlates with learning at the behavioral level. On average, dendritic CS responses increase in neurons with both up-regulated (CSup) or down-regulated (CSdown) somatic CS responses. However, fear conditioning also increases the variance of CS responses across the dendritic tree of a given neuron, indicating that not all dendrites are undergoing similar levels of plasticity during learning. Moreover, dendritic spines that show up-regulated CS responses are more likely to be located on dendrites that exhibit increased CS responses after learning. Last, even though dendritic CS responses of CSdown neurons are potentiated, their somatic responses are reduced by enhanced Parvalbumin-expressing (PV+) interneuron-mediated perisomatic inhibition, counteracting the learning-induced increased synaptic drive.

CONCLUSION: Our findings demonstrate that LA PNs locally integrate dendritic sensory inputs in a compartmentalized manner and that fear conditioning-induced plasticity of dendritic and somatic sensory responses can be uncoupled. Both compartmentalized dendritic integration and uncoupling of dendritic and somatic plasticity are regulated by local inhibitory circuits that specifically target dendrites or the perisomatic region, two distinct subcellular compartments of postsynaptic PNs. The regulation of compartmentalized dendritic and somatic plasticity increases the computational capacity of amygdala circuits, possibly enhancing an animal's behavioral flexibility in the face of danger. ■

The list of author affiliations is available in the full article online.

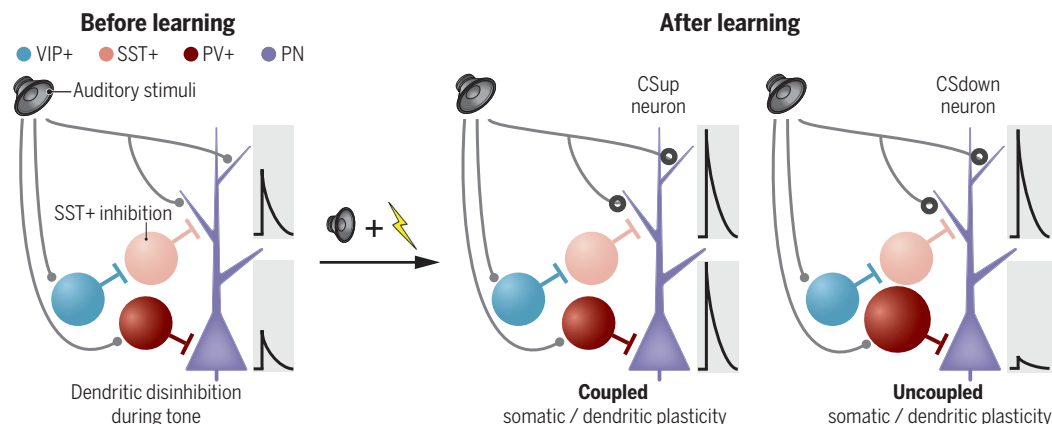
*Corresponding author. Email: andreas.luthi@fmi.ch

Cite this article as S. d'Aquin et al., *Science* **376**, eabf7052 (2022); DOI: 10.1126/science.abf7052

READ THE FULL ARTICLE AT
<https://doi.org/10.1126/science.abf7052>

Fear conditioning induces compartmentalized plasticity.

(Left) During auditory stimuli, dendritic disinhibition through SST+ interneurons amplifies dendritic Ca^{2+} responses. (Right) Fear conditioning induces a correlated increase of somatic and dendritic CS responses in a population of LA PNs (CSup neurons), whereas CSdown neurons show increased dendritic but decreased somatic CS responses. This compartmentalized plasticity is mediated by somatargeting PV+ interneurons.



RESEARCH ARTICLE

NEUROSCIENCE

Compartmentalized dendritic plasticity during associative learning

Simon d'Aquin^{1,2†}, Andras Szonyi^{1,3}, Mathias Mahn¹, Sabine Krabbe^{1†}, Jan Gründemann^{1,4†}, Andreas Lüthi^{1,2*}

Experience-dependent changes in behavior are mediated by long-term functional modifications in brain circuits. Activity-dependent plasticity of synaptic input is a major underlying cellular process. Although we have a detailed understanding of synaptic and dendritic plasticity *in vitro*, little is known about the functional and plastic properties of active dendrites in behaving animals. Using deep brain two-photon Ca^{2+} imaging, we investigated how sensory responses in amygdala principal neurons develop upon classical fear conditioning, a form of associative learning. Fear conditioning induced differential plasticity in dendrites and somas regulated by compartment-specific inhibition. Our results indicate that learning-induced plasticity can be uncoupled between soma and dendrites, reflecting distinct synaptic and microcircuit-level mechanisms that increase the computational capacity of amygdala circuits.

Dendrites are active neuronal compartments that dynamically integrate synaptic inputs and thereby affect a neuron's input-output function (1, 2). *In vivo* studies have shown that dendritic Ca^{2+} activity can be tuned to ongoing task variables (3, 4), in some cases even restricted to distinct dendritic branches (5–9). However, a large proportion of Ca^{2+} activity in behaving animals occurs in the form of global transients that involve both the somas and dendrites of single neurons, indicating a high degree of functional coupling between these compartments and emphasizing the importance of recording activity from dendrites and their parent somas simultaneously (10–12).

Recent studies focused mainly on dendritic activity in cortical regions, whereas the functional properties of dendrites in subcortical brain areas remain unexplored. The lateral amygdala (LA) is a subcortical brain structure central to classical auditory fear conditioning (FC), a fast and robust form of associative learning (13). During auditory FC, a tone conditioned stimulus (CS) is paired with an aversive unconditioned stimulus (US; typically a foot shock), which results in the induction of Hebbian activity-dependent synaptic plasticity at auditory synaptic inputs onto LA principal neurons (PNs) (14–18). A similar proportion of neurons up- and down-regulate their CS

response during learning (19–21). In addition, both plastic populations contained US responsive as well as US nonresponsive neurons, suggesting that FC involves more diverse forms of plasticity (22). However, these studies relied on somatic activity as readouts, whereas local dendritic activity and plasticity during associative learning was not explored.

Results

Deep brain imaging of tone and shock responses in LA neuron somas and dendrites in awake mice

To monitor somatic and dendritic activity in LA PNs, we virally expressed a Cre-dependent version of the Ca^{2+} sensor GCaMP6s together with highly diluted adeno-associated virus (AAV) expressing Cre recombinase under the calcium- and calmodulin-dependent protein kinase II (CaMKII) promoter and implanted a gradient-index (GRIN) lens above the virus injection site in the LA (Fig. 1, A to C; fig. S1A; and table S2). This resulted in sparse labeling of LA PNs with minimal background signal from out-of-focus sources when imaged with a two-photon microscope (Fig. 1, E and F, and movies S1 and S2). Somas and dendrites were registered and could be identified across multiple imaging sessions in awake mice, allowing reliable tracking of their activity across days (Fig. 1D).

The LA lacks a laminar organization, which makes challenging the association of dendritic branches with their parent soma. We therefore reconstructed the dendritic arbors of imaged neurons around the imaging plane on the basis of a three-dimensional (3D) structural scan acquired after completion of the behavioral experiments (Fig. 1G and fig. S2). To study associative fear learning, tones and mild electrical shocks are commonly used as

CS and US, respectively. Our approach allowed us to reliably record spontaneous activity as well as CS and US responses in somas and different dendritic compartments of individual, reconstructed LA PNs in awake mice (Fig. 1, H and I).

Global and local spontaneous somatic and dendritic activity

To investigate the extent of functional coupling between somas and dendrites, we detected Ca^{2+} transients in identified dendritic branches of single neurons and compared them with somatic transients (Fig. 2, A and C). The amplitude of simultaneous somatic and dendritic transients was correlated (Fig. 2D) (10, 11). Many of these dendritic transients may reflect back-propagating action potentials (bAPs) (Discussion). However, the strength of this correlation was reduced with increasing distance from the soma (Fig. 2E), indicating that activity in distal dendrites is more decorrelated from the soma. Overall, a small proportion of all dendritic Ca^{2+} transients in LA PNs (18.9% of 5227 transients detected in 113 dendrites from 13 neurons in six mice) were exclusive to dendritic branches, with no coincident Ca^{2+} event at the soma. Accordingly, the amplitude distribution of the somatic Ca^{2+} signals normalized to the maximal somatic signal magnitude and time locked to dendritic transients exhibited a bimodal distribution, with a peak around zero that reflects local dendrite-only transients and a second peak that reflects correlated somatic and dendritic transients (Fig. 2, F and G). The amplitude distribution of dendritic transients did not follow such a bimodal distribution (Fig. 2, H and I). The number and fraction of simultaneously active dendrites in a given cell was larger when dendrites were co-active with the soma as compared with when the soma was not active (Fig. 2, J to O).

Sensory stimulation generates local dendritic activity regulated by inhibition

We next examined soma-dendrite coupling during sensory stimulation in naïve animals. To check for differential sensory tuning in somas and dendrites, we presented mice with tones of varying frequencies and intensities as well as with electrical stimulation of different intensities (fig. S3, A to D). Although individual somas and dendrites exhibited a wide range of tuning properties, on average LA PNs responded stronger to high-intensity CS and US presentations compared with the stimuli with low intensity (fig. S3, B to D). Moreover, dendrites had similar tuning as that of their parent soma (fig. S3, E to G). However, the rate of dendrite-only Ca^{2+} transients was larger during tone presentations as compared with spontaneous activity in the absence of auditory input (Fig. 2P). Dendrite-specific Ca^{2+}

¹Friedrich Miescher Institute for Biomedical Research, Basel, Switzerland. ²University of Basel, Basel, Switzerland.

³Laboratory of Cellular Neurophysiology, Institute of Experimental Medicine, Budapest, Hungary. ⁴Department of Biomedicine, University of Basel, Basel, Switzerland.

*Corresponding author. Email: andreas.luthi@fmi.ch

†Present address: Institute of Pharmacology and Toxicology, University of Zürich, Zürich, Switzerland.

‡Present address: Deutsches Zentrum für Neurodegenerative Erkrankungen (DZNE), Bonn, Germany.

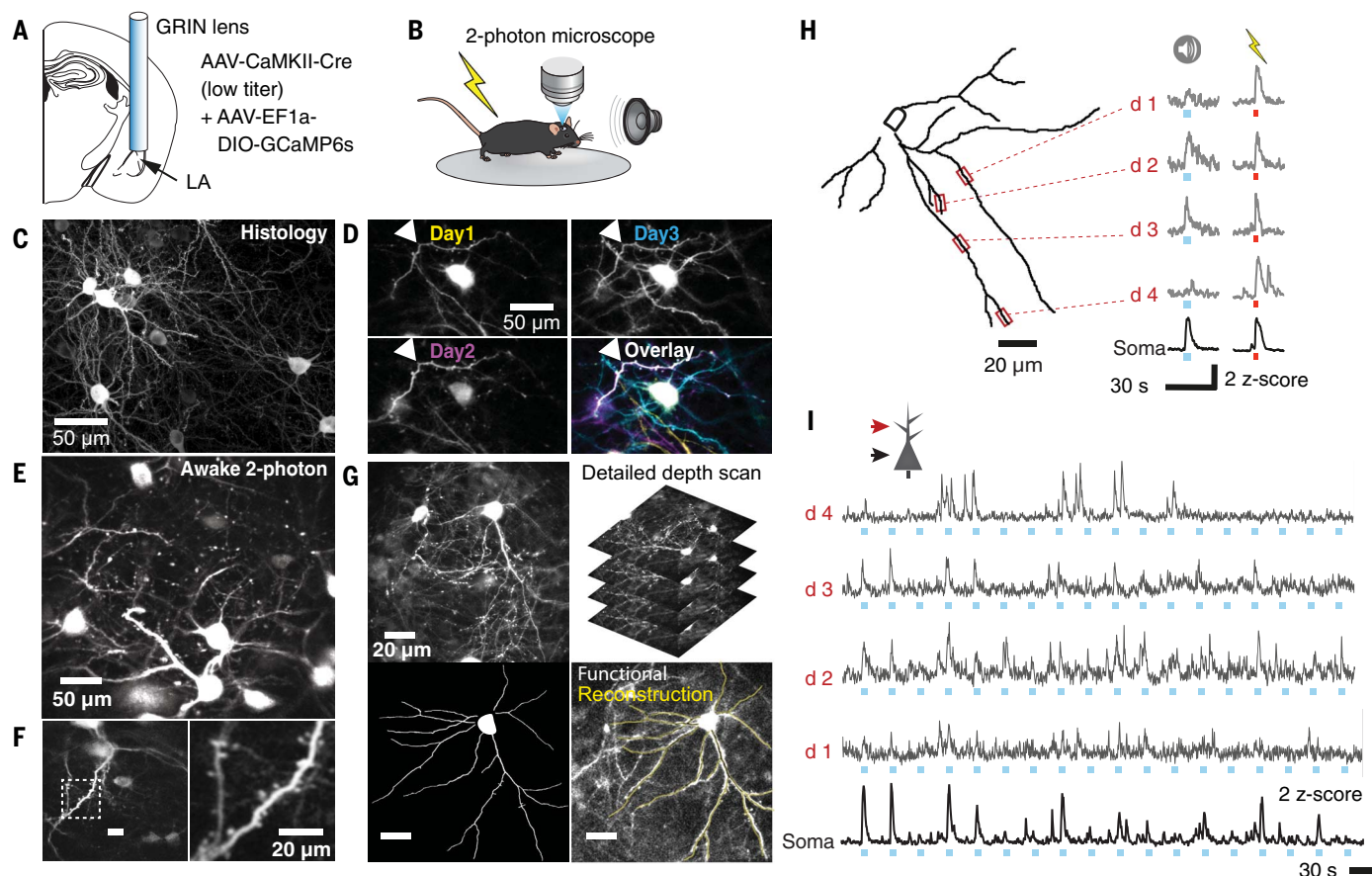


Fig. 1. In vivo dendritic calcium imaging in the LA. Experimental approach. (A) A highly diluted viral vector encoding CaMKII-Cre allows sparse but robust expression of GCaMP6s in LA PNs. A GRIN lens is implanted to gain optical access to the LA. (B) Head-fixed mice are allowed to run freely on a wheel under a two-photon microscope while presented with tone and shock stimuli. (C) Confocal image of sparsely infected LA PNs expressing GCaMP6s. (D) Imaging plane relocation in an awake mouse over 3 consecutive days. Each image was obtained by averaging 50 imaging frames recorded at 30 Hz. The white arrowhead indicates the same dendritic segment active over days. (Bottom right) Overlay of the 3 days, one color per

day. (E) Maximum intensity projection over a 15-min two-photon imaging session. (F) Deep brain imaging with dendritic spine resolution through a GRIN lens. The image was obtained by averaging 50 imaging frames recorded at 30 Hz. (G) Partial reconstruction of the dendritic arbor of imaged neurons. The dendrites of the imaged neurons were (bottom left) tracked in three dimensions on the basis of (top row) a structural scan acquired under anesthesia after the experiment and (bottom right) mapped back onto the functional imaging data. (H) Reconstruction of part of a LA PN dendritic tree. (I) Simultaneous Ca^{2+} imaging in the soma and dendrites of a LA PN. Shown is the same neuron as in (H). Blue rectangles indicate tones.

transients, but not dendritic Ca^{2+} transients coincidentally detected with somatic events, were stronger during tone presentations (Fig. 2, Q to T).

Similar to neocortical pyramidal cells, the activity of LA PNs is tightly controlled by local inhibitory interneurons. Somatostatin-positive (SST+) interneurons form γ -aminobutyric acid (GABA)-releasing synapses onto PN dendrites and are inhibited during CS and US presentations (23, 24), which suggests that SST+ interneurons can gate dendritic excitability of LA PNs during sensory stimulation (25). We thus reduced SST+ interneuron output by virally expressing the inhibitory DREADD (designer receptor exclusively activated by designer drugs) hM4D(Gi) while imaging LA PN activity during tone presentations (Fig. 3, A to C).

Chemogenetic inhibition of SST+ interneurons increased the rate and proportion of dendrite-specific Ca^{2+} transients (Fig. 3, D to

F) but had no further effect on tone-induced dendrite-specific Ca^{2+} transients, indicating that inhibition of SST+ interneurons leads to an increase in spontaneous, weak inputs that would otherwise be suppressed. Inhibition of SST+ interneurons led to an overall decrease in the amplitude correlation of dendritic and somatic transients (Fig. 3G). The rate and amplitude of somatic Ca^{2+} transients remained largely unaffected, with only a slight reduction in the somatic response integral (Fig. 3, H to J, and fig. S4, A to L).

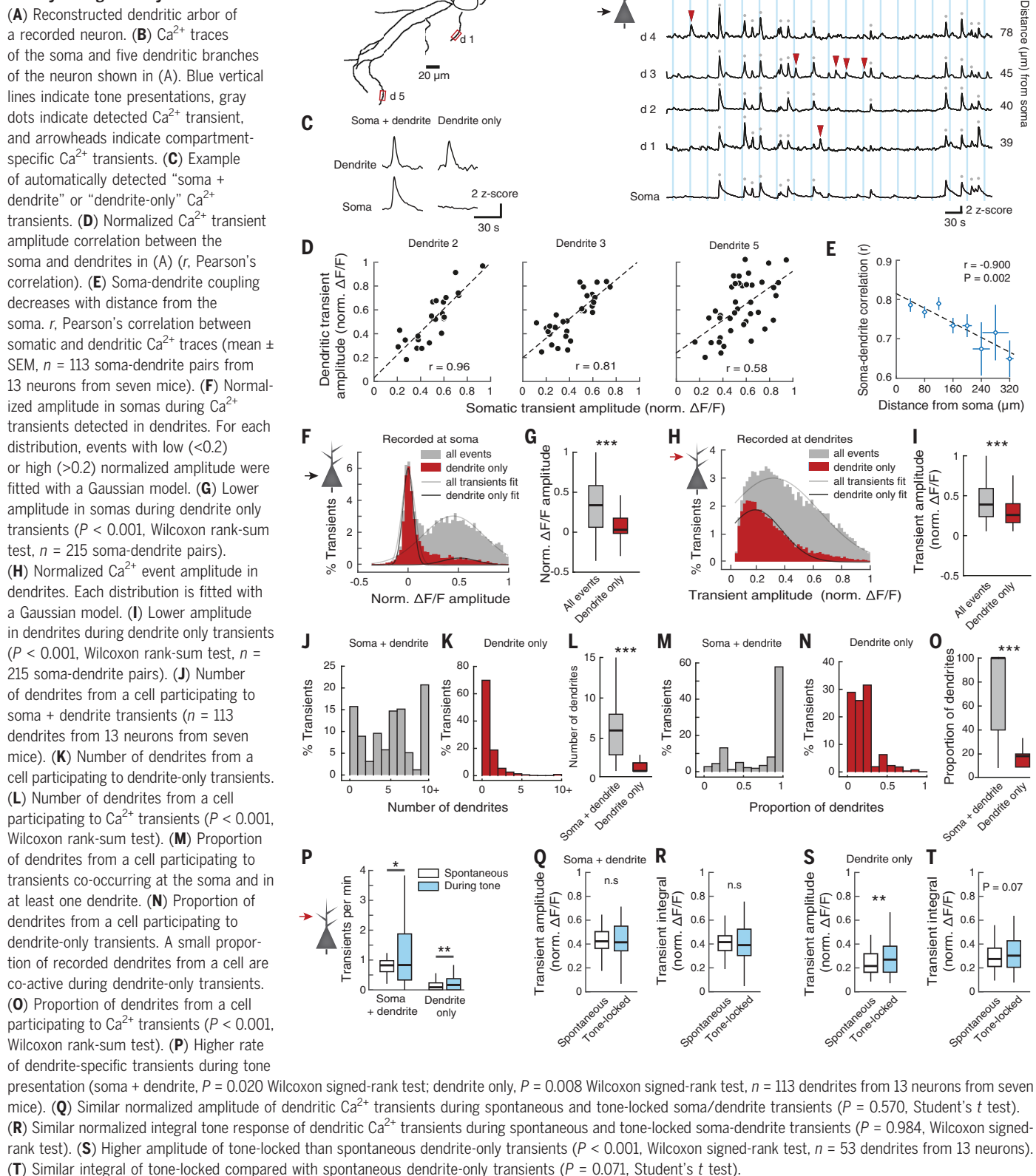
To address whether CS-induced inhibition of SST+ interneurons allows for the generation of dendritic CS responses during learning, we chemogenetically enhanced SST+ interneuron output during CS-US pairing while imaging LA PNs (Fig. 3K). In animals expressing hM3D(Gq) in SST+ interneurons, clozapine N-oxide (CNO) administration during conditioning led to a reduction in dendritic CS

response magnitude relative to CS responses measured in LA PNs during the preceding habituation session (fig. S4, N to T). This effect was even more pronounced when selectively analyzing PN dendrites and somas that showed CS responses during the habituation session (Fig. 3, L to O). Application of CNO in control animals only expressing mCherry did not reduce CS response magnitude (Fig. 3, P to T).

Associative FC induces bidirectional plasticity of somatic CS responses

One-photon Ca^{2+} imaging experiments indicate that FC induces a bidirectional plasticity of somatic CS responses in BLA PNs and that CS responses can be potentiated even in cells that do not exhibit US responses at the soma (19, 27). Assuming that somatic plasticity reflects, to a large extent, plasticity at the synaptic and dendritic level, we sought to investigate FC-induced changes in CS responses at the subcellular level.

Fig. 2. Increased dendrite-specific activity during auditory stimulation.



To better interpret changes in sensory stimulus representation after learning, we first examined the stability of somatic CS responses

across days in naïve animals under head-fixed two-photon imaging conditions. The somatic tone responsiveness was strongly conserved

on up to 4 consecutive days, indicating a high cross-day stability of CS responses in LA PN of nonconditioned animals (fig. S5).

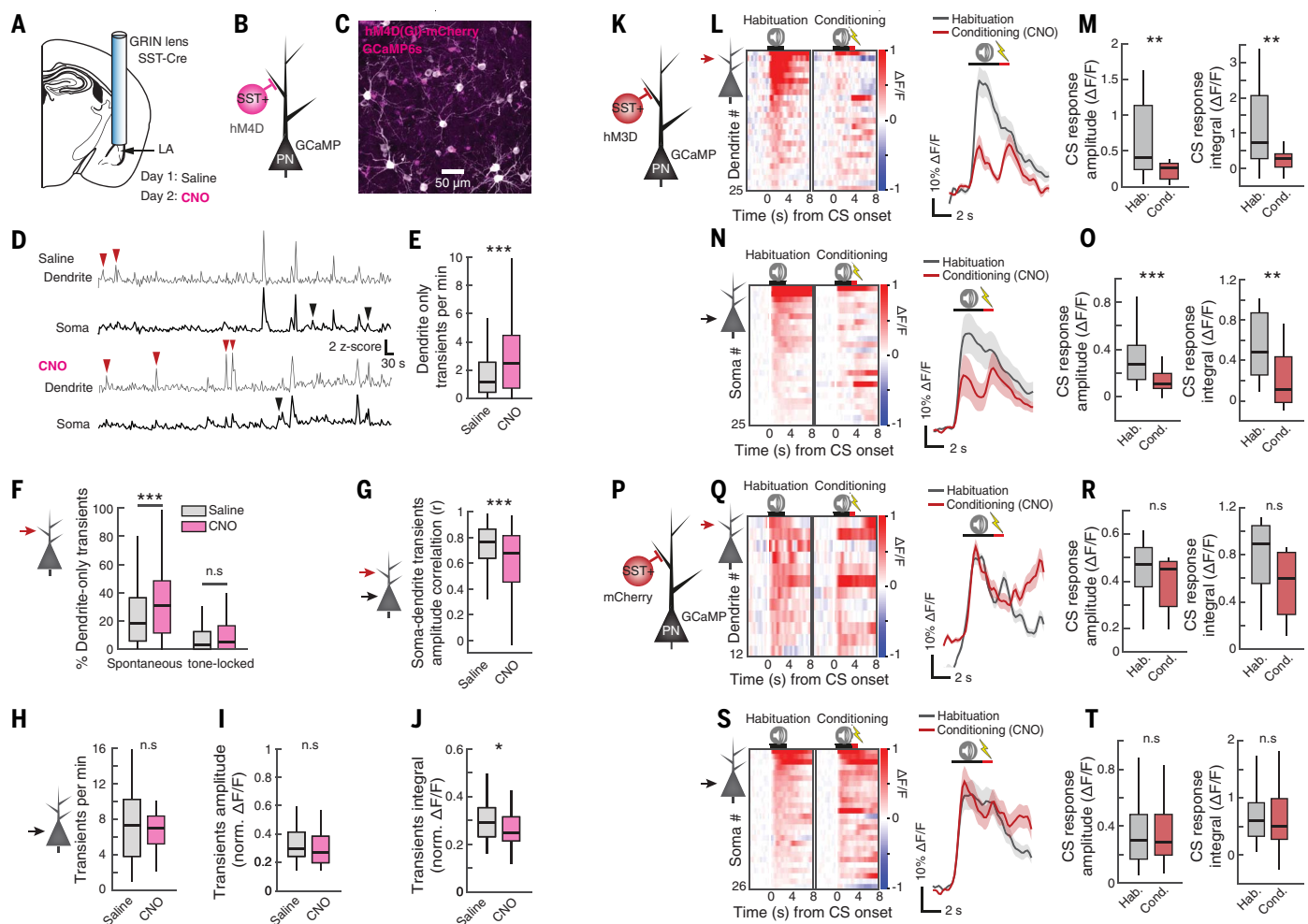


Fig. 3. SST+ interneurons control dendritic activity and CS responses.

(A) Viral approach to express hM4D(Gi) in SST+ INs and GCaMP6s in a sparse population of LA PNs. Ninety tones were presented after saline or intraperitoneal injection of CNO on 2 consecutive days. **(B)** Experiment scheme. **(C)** Confocal image of hM4D(Gi)-mCherry in SST+ INs with sparse GCaMP6s in LA PNs. **(D)** Reduction of SST+ IN output increases dendrite-only transients. Arrowheads indicate compartment-specific transients in an example soma-dendrite pair. **(E)** Reduction of SST+ IN output increases the rate of dendrite-only transients ($P < 0.001$ Wilcoxon signed-rank test, $n = 79$ dendritic segments, 14 neurons). **(F)** Reduction of SST+ IN output increases spontaneous, but not tone-locked, dendrite-only transients (Spontaneous, $P < 0.001$; tone-locked, $P = 0.125$, Wilcoxon signed-rank test). **(G)** Reduction of SST+ IN output reduces the amplitude correlation between somatic and dendritic transients (r , Pearson's correlation coefficient, $P < 0.001$ Wilcoxon signed-rank test). **(H)** Reduction of SST+ IN output does not change the rate of somatic transients ($P = 0.347$, Wilcoxon signed-rank test, $n = 30$ neurons). **(I)** Reduction of SST+ IN output does not change the amplitude of somatic transients ($P = 0.140$, Student's t test). **(J)** Reduction of SST+ IN output decreases the integral of somatic transients ($P = 0.022$, Student's t test). **(K)** Experimental scheme. **(L)** (Left) CS responses

ordered according to amplitude during habituation. (Right) Mean responses \pm SEM ($n = 25$ CS-responsive dendrites during habituation, five mice). **(M)** Statistical analysis of (L). (Left) CS response $\Delta F/F$ amplitude ($P = 0.002$ Wilcoxon matched-pairs signed-rank test). (Right) CS response $\Delta F/F$ integral ($P = 0.705$ Wilcoxon matched-pairs signed-rank test; conditioning, 0.307 ± 0.096 $\Delta F/F$ integral). **(N)** (Left) CS responses ordered according to amplitude during habituation. (Right) Mean responses \pm SEM ($n = 25$ CS-responsive somas during habituation, 5 mice). **(O)** Statistical analysis of (N). (Left) CS response $\Delta F/F$ amplitude ($P < 0.001$ Wilcoxon matched-pairs signed-rank test). (Right) CS response $\Delta F/F$ integral ($P = 0.002$ Wilcoxon matched-pairs signed-rank test). **(P)** Experimental scheme. **(Q)** (Left) CS responses ordered according to amplitude during habituation. (Right) Mean responses \pm SEM ($n = 12$ CS-responsive dendrites during habituation, four mice). **(R)** Statistical analysis of (Q). (Left) CS response $\Delta F/F$ amplitude ($P = 0.979$ Student's t test). (Right) CS response $\Delta F/F$ integral ($P = 0.733$ Wilcoxon matched-pairs signed-rank test). **(S)** (Left) CS responses ordered according to amplitude during habituation. (Right) Mean responses \pm SEM ($n = 26$ CS-responsive somas during habituation, four mice). **(T)** Statistical analysis of (S). (Left) CS response $\Delta F/F$ amplitude ($P = 0.585$ Student's t test). (Right) CS response $\Delta F/F$ integral ($P = 0.568$ Wilcoxon matched-pairs signed-rank test).

We then performed a 3-day differential auditory FC paradigm in a separate group of mice while recording somatic and dendritic Ca^{2+} activity in head-fixed mice under a two-photon microscope (Fig. 4A). Animals exhibited increased levels of freezing behavior when

exposed to the CS 24 hours after FC under freely moving conditions before imaging Ca^{2+} responses (Fig. 4B). In these animals ($n = 9$), we imaged in total 177 neurons, 82% of which showed CS responses before or after conditioning, whereas 18% of all neurons were not

CS responsive (fig. S6C). Compared with pre-conditioning levels, 84% of all CS responsive neurons (123 neurons from nine animals) exhibited learning-associated plasticity of CS responses, whereas 13% showed stable CS responses (fig. S6C).

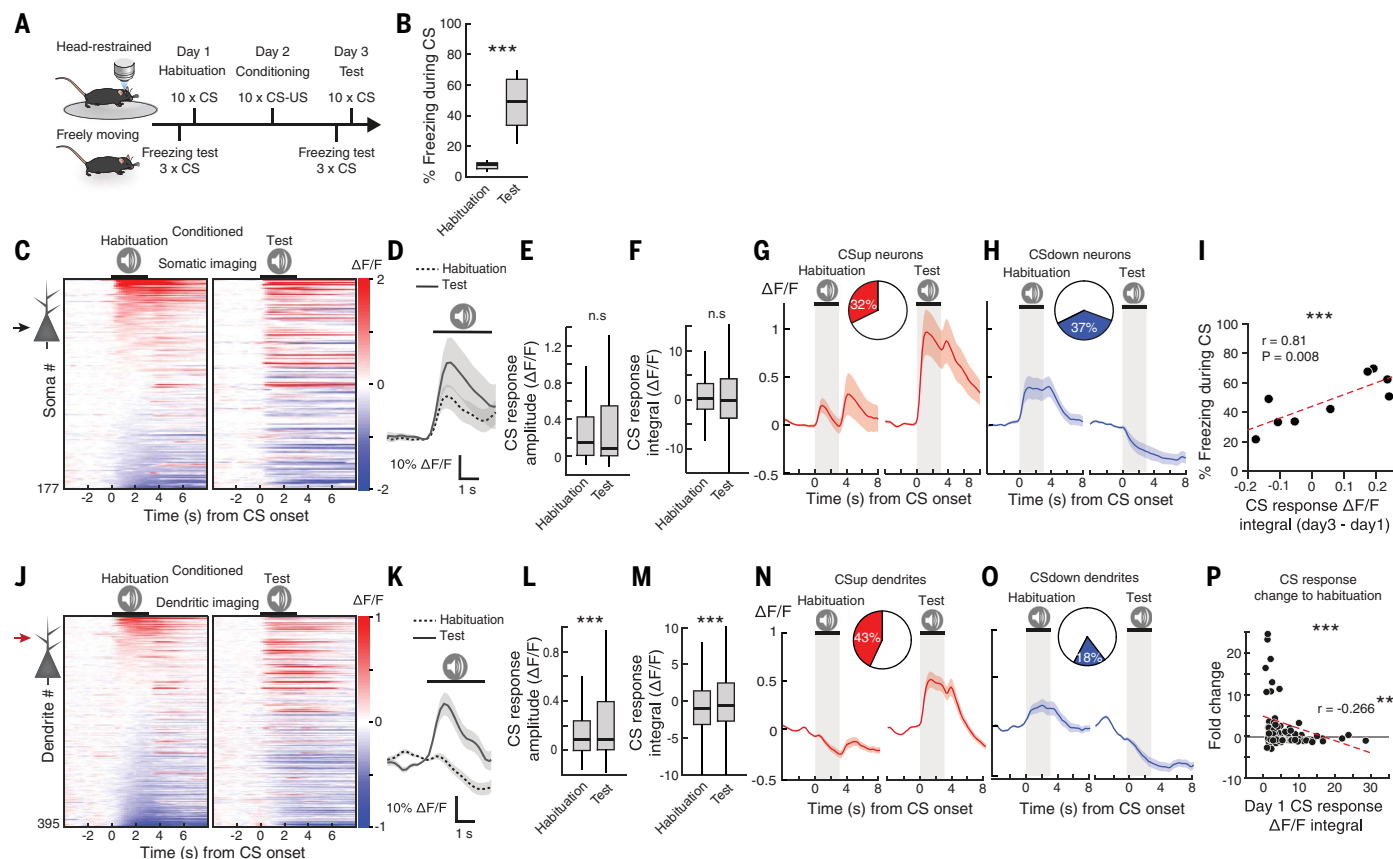


Fig. 4. CS response dynamics in LA somas and dendrites during auditory FC. (A) Auditory FC paradigm with simultaneous two-photon imaging. Freezing tests were performed in freely moving conditions. (B) Mice learn the CS-US association. Shown is percent time spent freezing, during the CS before and after learning ($P < 0.001$, Wilcoxon signed-rank test; habituation, $n = 6$ mice; test, $n = 9$ mice). (C) CS responses in somas before and after FC ordered according to amplitude during habituation ($n = 177$ somas from nine mice). (D) Mean somatic CS response before and after FC ($n = 177$ somas from nine mice, mean \pm SEM). (E) The mean somatic CS response amplitude is similar before and after FC ($P = 0.641$ Wilcoxon signed-rank test). (F) The mean somatic CS response integral is similar before and after FC ($P = 0.547$ Wilcoxon signed-rank test). (G and H) A large proportion of somas (G) up-regulate and (H) down-regulate their CS response upon FC (mean \pm SEM). (I) Time spent freezing during CS is correlated with somatic CS response integral change after FC (r , Pearson's

correlation, $P = 0.008$, $n = 177$ somas, 19.6 ± 5.4 neurons per mouse from nine mice). (J) CS responses in dendrites before and after FC ordered according to amplitude during habituation ($n = 395$ dendrites from nine mice). (K) Mean CS response of all dendrites before and after FC (mean \pm SEM). (L) The mean dendritic CS response amplitude increases after FC ($P < 0.001$ Wilcoxon signed-rank test). (M) The mean dendritic CS response integral increases after FC ($P < 0.001$ Wilcoxon signed-rank test, $n = 395$ dendrites from nine mice). (N) A large proportion of dendrites up-regulate and (O) a smaller proportion down-regulate their CS response after FC (mean \pm SEM). (P) Dendritic CS response fold change after paired conditioning normalized to habituation. The median response integral is similar ($P = 0.172$ one-sample Wilcoxon signed-rank test, $173 \pm 57\%$ CS response integral increase). The CS response integral is anticorrelated to the CS response integral during habituation (r , Pearson's correlation coefficient, $n = 97$ dendrites from nine mice).

Whereas the overall average somatic CS-response magnitude remained similar after FC (Fig. 4, C to F), neurons could be subdivided into three functional subpopulations: neurons exhibiting increased CS responses (CSup neurons; 32% of $n = 57$ of all neurons from $n = 9$ animals), neurons exhibiting decreased CS responses (CSdown neurons; 37% of all neurons), and neurons with stable CS responses (Fig. 4, G and H).

Similar proportions of CSup and CSdown neurons were US responsive or US nonresponsive ($P = 0.527$, Fisher's exact test) (fig. S6, F and G), indicating that somatic US responsiveness is not necessary for CS response plasticity, nor does it predict the direction of plasticity.

To test the specificity of the observed FC-induced plasticity of CS responses, we subjected mice to an unpaired conditioning paradigm, in which the CS and the US were presented independently (more than 120 s apart) (fig. S7). Unpaired conditioned mice did not freeze when exposed to the CS (fig. S7B). Consequently, unpaired conditioning resulted in an overall reduction of somatic CS response amplitudes at the population level (fig. S5, C to F, and fig. S9).

Comparing the proportions of CSup and CSdown neurons between naïve mice and mice subjected to associative conditioning or unpaired conditioning protocols revealed that CSup neurons were overrepresented in conditioned mice relative to mice subjected to

unpaired conditioning ($P < 0.001$, Fisher's exact test), whereas CSdown neurons were found in similar proportions in animals that underwent paired or unpaired conditioning ($P = 0.247$, Fisher's exact test) (Fig. 4, G and H, and fig. S7, G and H).

The absolute CS response change during auditory FC strongly correlated with acquired freezing behavior after conditioning in animals subjected to paired (Fig. 4I), but not unpaired, conditioning (fig. S7I), which suggests that updating of CS response representations is necessary for conditioned freezing behavior (21). This correlation relied on both CSup and CSdown neuron activity (fig. S7, Q and R), which suggests that both CS response

plasticity types contribute to the new CS representation in the amygdala after conditioning.

Associative FC induces differential somatic and dendritic plasticity

We next examined FC-induced dendritic plasticity. In total, we imaged 395 dendrites (from nine animals), 75% of which showed CS responses before or after conditioning, whereas 25% of all dendrites were not CS responsive. Compared with preconditioning levels, 87% of all CS responsive dendritic segments (258 dendritic segments from nine animals) exhibited learning-associated plasticity of CS responses, whereas 13% showed stable CS responses (fig. S6C).

Overall, FC induced both up- and down-regulation of CS responses in dendrites (Fig. 4, J, N, and O). However, in contrast to somatic plasticity, FC resulted in an overall net increase in dendritic CS responses (Fig. 4, K to M) driven by a large fraction of CSup dendrites (43%), with only a relatively small fraction of CSdown dendrite (18%) (Fig. 4, N to P). There was a higher proportion of CSup than CSdown dendritic segments, in contrast to the almost equal proportions observed at the somatic level (fig. S6C).

To assess whether the overall potentiation of dendritic CS responses was specific for associative FC, we analyzed dendritic CS response plasticity in mice subjected to an unpaired conditioning paradigm. The dendritic CS response was decreased in unpaired conditioned animals (fig. S7, K to M). These results were robust to normalization to the mean initial CS response amplitude between groups (fig. S10). Similar to the changes of somatic CS responses upon unpaired conditioning, there was a large fraction of CSdown dendrites (35%), with only a minor population of CSup dendrites (7%) (fig. S7, N to P).

CS response plasticity in dendritic spines

Consistent with the large fraction of CSup dendrites, CS responses of dendritic spines were on average increased (fig. S8, A to E). Similar to somatic and dendritic responses, spines showed CSup and CSdown plasticity patterns (fig. S8, F to I). In total, we recorded 112 spines on identified CSup dendrites and 28 spines on identified CSdown dendrites. On average, CSup dendrites exhibited more spines with increased CS responses (CSup spines) than spines with decreased CS responses (CSdown spines) (fig. S8J). By contrast, CSup spines were underrepresented on CSdown dendrites (fig. S8K).

Consistent with the idea of anatomical clustering of dendritic spines with a conditioning-induced increase in their CS responses (CSup spines), the distance between CSup spines located on a given dendritic branch was found to be smaller as compared with the distance

between CSdown spines (fig. S8L). Last, our results indicate that US-responsive dendrites contain a comparatively larger fraction of CSup spines, whereas US-unresponsive dendrites contain more CSdown spines (fig. S8M).

Subcellular compartment-specific plasticity in single neurons

Given the variability of soma-dendrite correlation in single neurons (Fig. 2, B and D), we next examined whether learning would change the variability of CS responses between individual dendritic branches belonging to the same neuron. CS response plasticity was variable between the different dendritic branches of single neurons (Fig. 5, A, B, and G), and somatic and dendritic activity became more decorrelated after FC (Fig. 5, C and D). The amplitude decorrelation of somatic and dendritic transients was more pronounced in dendrites located several branch points away from the soma—third order or higher as compared with first- and second-order branches (fig. S9B). However, we did not observe a linear effect of distance from soma on transient amplitude correlation (fig. S9A).

The overall probability of a CS input to trigger local, dendrite-only transients was increased upon learning (Fig. 5E), but the number and proportion of dendrites co-active during somatic activity did not change upon conditioning (fig. S9, C to P), indicating that plasticity of CS responses can be restricted to individual dendritic branches. In contrast to CS-evoked responses, the proportion of dendrite-only events during spontaneous activity did not change upon FC (fig. S9, Q to S).

Dendritic CS response variability increased in conditioned mice but was not observed upon unpaired conditioning (Fig. 5G), suggesting that associative learning specifically induces decorrelation of somatic and dendritic CS responses.

Most dendrites of somatically US-responsive neurons also exhibited US responses (44 of 79 dendrites, 56%). Localized dendritic US responses were also present in some dendrites of neurons that lacked somatic US responses (35 of 158 dendrites, 22%) (fig. S6, H and I), suggesting that dendrite-specific US responses might still influence CS response plasticity at the soma.

To examine how dendritic CS response plasticity relates to somatic plasticity in single neurons, we compared the plasticity of individual dendritic branches with somatic plasticity in identified CSup and CSdown neurons (Fig. 5, H to S). The amplitude of dendritic CS responses increased in CSup neurons (Fig. 5, N to P). By contrast, dendritic and somatic CS response plasticity was uncoupled in CSdown neurons. Whereas the mean amplitude of somatic CS responses was decreased in CSdown neurons, CS responses increased in the den-

drates of the same neurons (Fig. 5, Q to S), indicating that the cellular mechanisms underlying CS response plasticity in CSup and in CSdown neurons are fundamentally different.

Perisomatic inhibition uncouples dendritic and somatic CS response plasticity

One possible mechanism that might underlie the uncoupling of somatic and dendritic CS response plasticity observed in CSdown neurons could be a conditioning-induced increase in perisomatic inhibition (26). In the LA, like in the cortex or hippocampus, parvalbumin (PV)-expressing interneurons mediate perisomatic inhibition and tightly control PN activity (21). To investigate the effect of PV+ interneurons on somatic CS response plasticity, we chemogenetically suppressed their activity (Fig. 6, A to C). Inhibition of LA PV+ interneurons led to a reduced inhibitory drive onto PNs *in vitro* (Fig. 6, D to F) and to an increased rate of somatic Ca^{2+} transients in PNs *in vivo* (Fig. 6G). Inhibition of PV+ interneurons during memory retrieval (test session) 24 hours after FC decreased the proportion of CSdown neurons compared with that in control animals, without any effect on the proportion of CSup neurons (Fig. 6J). In the remaining CSdown neurons that we detected while inhibiting PV+ interneurons, the CS response amplitude decreased, however, to a lesser extent than in the control group, whereas CS response amplitudes increased similarly in CSup neurons (Fig. 6, K to N).

Discussion

We used *in vivo* chronic two-photon Ca^{2+} imaging to investigate dendritic function and plasticity in LA PNs. Under baseline conditions, somatic and dendritic Ca^{2+} transients were strongly coupled. Recent studies in the neocortex reported that the fraction of Ca^{2+} transients restricted to dendrites is relatively small (10–12). Pervasive global Ca^{2+} transients could reflect efficient somatic AP back-propagation into the dendritic arbor of LA PNs (10, 27). However, the temporal resolution of the currently available Ca^{2+} sensors does not permit to determine the temporal sequence and causality of somatic and dendritic activity. Nonetheless, in the LA the correlation between the amplitude of co-occurring somatic and dendritic Ca^{2+} transients was variable and decreased with increasing distance from the soma within single neurons, and local dendritic activity occurred independently from somatic activity (Fig. 2). The rate and amplitude of dendrite-specific Ca^{2+} transients was notably higher during auditory sensory stimulation (Fig. 2, P and S), indicating that dendrites of LA PNs locally integrate auditory inputs.

In cortex and in the basolateral amygdala (BLA), dendritic activity is thought to be regulated by dendrite-targeting interneurons

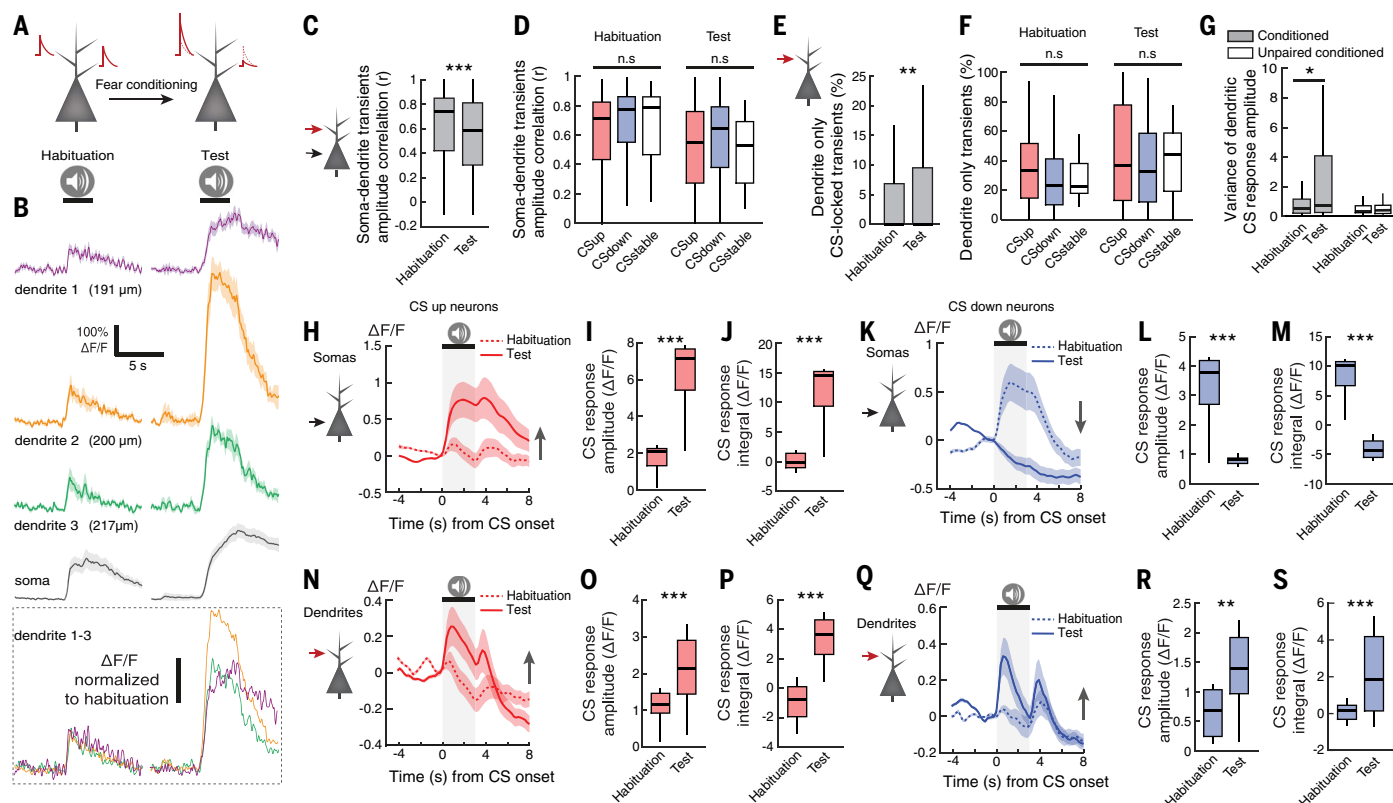


Fig. 5. Uncoupling of somatic and dendritic plasticity of CS response upon auditory FC. (A) Simultaneous imaging of the soma and dendrites. (B) Variability of CS response between the soma and three dendritic segments of a neuron before and after FC (mean \pm SEM). (Bottom) CS responses normalized to habituation day. (C) Correlation of soma-dendrite event amplitude decreases after FC (r , Pearson's correlation coefficient, $P < 0.001$ Wilcoxon signed-rank test, $n = 262$ soma-dendrite pairs, 34 neurons). (D) Correlation of soma-dendrite transient amplitudes is similar between CSup, CSdown, and CSstable neurons [r , Pearson's correlation coefficient, habituation: $F(2, 185) = 2.34$, $P = 0.099$; test: $F(2, 185) = 1.74$, $P = 0.179$; both one-way ANOVA; $n = 69$ soma-dendrite pairs, 15 CSup neurons, 199 soma-dendrite pairs, 21 CSdown neurons, 19 soma-dendrite pairs, seven CSstable neurons]. (E) The proportion of CS-locked dendrite-only transients increases after FC ($P = 0.008$ Wilcoxon signed-rank test, $n = 262$ soma-dendrite pairs, 34 neurons). (F) The proportion of CS-locked dendrite-only transients is similar between CSup, CSdown, and CSstable neurons [habituation, $F(2, 185) = 2.34$, $P = 0.099$; test, $F(2, 185) = 1.74$, $P = 0.179$; both one-way ANOVA]. (G) The variance of CS response amplitude increases between dendrites after FC ($P = 0.010$, both

Student's t test, $n = 250$ dendrites, 50 neurons, nine mice). (H) Mean CS response increases in CSup somas after FC ($n = 19$ neurons, mean \pm SEM). (I) CS response amplitude increases in CSup somas after FC ($P < 0.001$, Wilcoxon signed-rank test). (J) CS response integral increases in CSup somas after FC ($P < 0.001$, Student's t test). (K) Mean CS response decreases in CSdown somas after FC ($n = 18$ neurons, mean \pm SEM). (L) CS response amplitude decreases in CSdown somas after FC ($P < 0.001$, Wilcoxon signed-rank test). (M) CS response integral decreases in CSdown somas after FC ($P < 0.001$, Wilcoxon signed-rank test). (N) Mean CS response increases in the dendrites of CSup neurons after FC ($n = 110$ dendrites, mean \pm SEM). (O) CS response amplitude increases in the dendrites of CSup neurons after FC ($P < 0.001$, Wilcoxon signed-rank test). (P) CS response integral increases in the dendrites of CSup neurons after FC ($P < 0.001$, Student's t test). (Q) Mean CS response increases in the dendrites of CSdown neurons after FC ($n = 70$ dendrites, mean \pm SEM). (R) CS response amplitude increases in the dendrites of CSdown neurons after FC ($P = 0.004$ Wilcoxon signed-rank test). (S) CS response integral increases in the dendrites of CSdown neurons after FC ($P = 0.002$, Student's t test).

(28–30). SST+ interneurons, in particular, predominantly contact PN dendrites and provide input-specific inhibition to PNs. SST+ interneurons in the BLA are inhibited during CS presentation, putting them in an ideal position to control dendritic excitability and gate dendritic integration and plasticity (23, 24). CS-induced inhibition of SST+ interneurons is necessary for learning (24). We found that dendrite-specific Ca^{2+} transients are under the control of SST+ interneurons in vivo and that silencing of SST+ interneurons increases dendrite-specific transients without affecting somatic activity in PNs (Fig. 3, E to J). Moreover, SST+ interneurons suppress spontaneous, less salient inputs to PN dendrites

(Fig. 3F). The relief of SST+ interneuron-mediated dendritic inhibition is necessary for the generation of dendritic CS responses during conditioning (Fig. 3, L and M). This is consistent with the notion that disinhibition through SST+ interneurons creates a temporal window that allows for the induction of dendritic plasticity during the coincident US (23, 24).

Upon FC, the somatic CS response of LA PNs remained stable on the population level (Fig. 4, D to F). However, single-neuron dynamics revealed that bidirectional plasticity of somatic CS responses (Fig. 4, G and H) and freezing behavior was correlated with the absolute somatic CS response change (Fig. 4I),

suggesting that CSup and CSdown neurons contribute not only to CS discrimination (27) but also to conditioned freezing behavior after FC. Our observation that the correlation between CS response plasticity and conditioned freezing behavior depended on both CSup as well as CSdown neurons may suggest that these two populations might function in concert to induce appropriate behavioral responses.

By contrast, LA PN dendrites and spines predominantly up-regulated their CS response upon FC (Fig. 4, K to M and P, and fig. S8, A to E), indicating, on average, a higher proportion of potentiated CS responses in dendrites. These changes were specifically induced in animals presented with temporally contingent

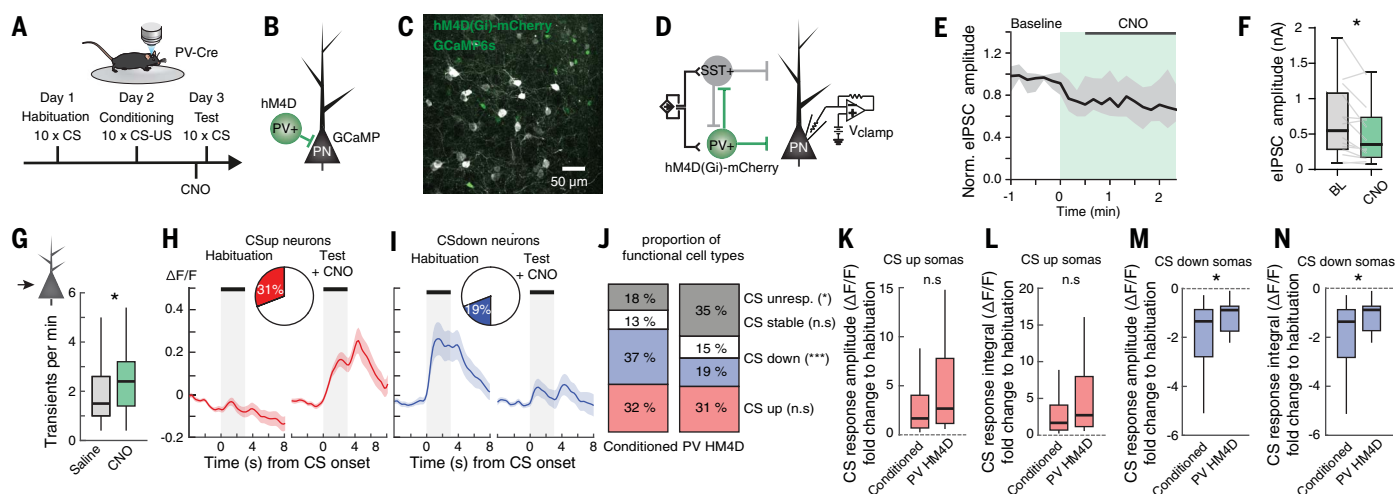


Fig. 6. Uncoupling of dendritic and somatic plasticity in CSdown neurons is mediated by an increase in perisomatic inhibition. (A) Auditory FC paradigm with simultaneous two-photon imaging. (B) Experiment scheme. (C) Confocal microscopy image of hM4D(Gi)-mCherry in PV+ INs with sparse GCaMP6s in LA PNs. (D) Whole-cell recording of evoked inhibitory postsynaptic current (eIPSC) in BLA PNs. (E) Reduction of PV+ IN output effect on eIPSC amplitude in BLA PNs ($n = 14$ cells, three mice). Median (black) and interquartile range (gray) are normalized to median baseline period. Green shaded area indicates bath application of CNO. Top black line indicates the CNO analysis window. (F) Statistical analysis of (E) ($P = 0.017$, Wilcoxon matched-pairs signed-rank test). (G) Suppression of PV+ IN output increases the rate of somatic transients ($P = 0.012$, one-sample Wilcoxon signed-rank test, $n = 66$ neurons). (H) A large proportion of somas up-regulate and others (I) down-regulate their CS response after FC (mean \pm SEM). (J) Similar proportion of CSup and smaller

proportion of CSdown somas in mice with suppressed PV+ IN activity in the amygdala (CSup, $P = 0.618$; CSdown, $P < 0.001$; both Fisher's exact test, Bonferroni corrected; conditioned, $n = 177$ neurons from nine mice; PV CNO, $n = 66$ neurons from six mice). (K) Reduction of PV+ IN output does not affect CS response amplitude change in CSup neurons during auditory FC ($P = 0.552$ Wilcoxon rank-sum test; conditioned, $n = 57$ neurons; PV CNO, $n = 39$ neurons). (L) Reduction of PV+ IN output does not affect CS response integral change in CSup neurons during auditory FC ($P = 0.622$ Wilcoxon rank-sum test; conditioned, $n = 57$ neurons; PV CNO, $n = 39$ neurons). (M) Reduction of PV+ IN output decreases the CS response amplitude change of CSdown neurons after auditory FC ($P = 0.039$ Wilcoxon rank-sum test; conditioned, $n = 66$ neurons; PV CNO, $n = 27$ neurons). (N) Reduction of PV+ IN output decreases the CS response integral change of CSdown neurons after auditory FC ($P = 0.032$, Wilcoxon rank-sum test; conditioned, $n = 66$ neurons; PV CNO, $n = 27$ neurons).

CS-US pairings. By contrast, in unpaired conditioned mice exposed to equal CSs and USs, but in a temporally unpaired manner, CS responses of somas and dendrites decreased uniformly (fig. S7, C to F and J to M). CS-US pairing thus induces dendritic plasticity of CS responses that is not fully reflected at the level of the soma. To explore the relationship between somatic and dendritic CS response plasticity at the single-neuron level, we simultaneously examined conditioning-induced changes in somas and in connected dendrites. Consistent with the population-level analysis and with previous one-photon imaging results from populations of amygdala neurons in freely moving animals (20, 21), we found that LA PN somas could be divided into three functional plasticity types with either increased, decreased, or unchanged CS responses. Only a minority of CSup and CSdown somas exhibited converging CS and US responses during conditioning, indicating that both the up-regulation and the down-regulation of somatic responses may result from different induction processes involving synaptic and/or dendritic plasticity as well as network effects.

Our finding that individual dendritic branches can exhibit US responses that do not result in somatic transients and are uncoupled from somatic activity suggests that conditioning

may lead to local, compartmentalized plasticity in dendrites that might encode the CS-US association memory in the BLA (27). CSup and CSdown spines are preferentially located on CSup and CSdown dendrites, respectively (fig. S8). Further, consistent with the idea of anatomical clustering of potentiated synaptic inputs (31), the distance between CSup spines located on a given dendritic branch is smaller as compared with the distance between CSdown spines (fig. S6L). Therefore, conclusions based on somatic US responses may underestimate the complexity of dendritic integration and plasticity as a source of neuronal output adaptation and learning (32), as suggested by a recent computational modeling study (33).

We observed that FC resulted in a decorrelation of CS responses between dendrites and their parent soma, as well as between individual dendritic branches belonging to the same neuron (Fig. 5, B, C, and E). This may reflect conditioning-induced and branch-specific changes in action potential backpropagation, possibly resulting from changes in SST+ interneurons-mediated dendritic inhibition. More likely, FC might lead to the induction of localized synaptic and dendritic CS response plasticity. The more pronounced decorrelation observed in more distal, higher-order dendrites (Fig. 5C) argues for local dendritic plasticity

as the origin of soma-dendrite decorrelation than for alterations in action potential backpropagation that would increase soma-dendrite correlations. Moreover, although the proportion of dendrite-only CS responses increased after FC (Fig. 5E), the overall proportion of spontaneous dendrite-only Ca^{2+} transients did not change (fig. S9, Q to S). This suggests that FC does not lead to a general increase in dendritic excitability but specifically increases dendritic responses to the conditioned sensory inputs (34).

Whereas dendrites and their parent soma of CSup neurons generally exhibited a correlated increase in their CS responses after learning, this was not the case for CSdown neurons. Even though the somas of CSdown neurons showed decreased CS responses upon learning, dendrites belonging to the same neurons did not but instead exhibited increased CS responses. This strongly suggests that in CSdown neurons, learning-induced dendritic and somatic plasticity mechanisms are distinct from CSup neurons.

Although increased dendritic responses in CSdown neurons likely result from potentiation of synaptic inputs, decreased somatic responses may reflect soma-specific changes of neuronal excitability (35–37) and/or plasticity of local soma-targeting inhibitory circuits (28, 38).

In support of the latter, suppressing the activity of soma-targeting PV+ interneurons reduced the proportion of CSdown neurons after FC (Fig. 6J), thus suggesting that in CSdown neurons, increased perisomatic inhibition counteracts excitatory dendritic inputs (39). Consistent with this, somatic inhibition undergoes anatomical and functional plasticity upon FC, resulting in a network-wide remodeling of the excitation/inhibition balance (26, 40).

Stimulus-specific dendritic response strengthening along with changes in stimulus-specific somatic inhibition could be a hallmark of network reorganization during the formation of new associations that allow stimulus-specific behavioral responses or the regulation of stimulus discrimination after learning or contribute to circuit homeostasis (21, 41, 42). Classical Hebbian learning models neither consider the contribution of inhibitory interneurons and the subcellular compartments they target nor the differential plasticity of distinct neuronal compartments and therefore fail to appropriately describe effects on the level of local microcircuits (43, 44). It is still unclear which factors determine the direction of plasticity in single neurons. Studies point to the importance of a neuron's intrinsic excitability at the time of memory formation (45), its afferent inputs and/or output targets (18, 46, 47), the role of inhibitory interneurons (23, 24, 38), and the clustering of synaptic inputs along the dendritic arbor (38, 48). Future experiments studying how specific long-range inputs and inhibitory microcircuits control somato-dendritic coupling as well as compartment-specific signal integration and plasticity might reveal general principles of network reorganization underlying the encoding and storage of newly formed memories.

Materials and methods

Animals

All animal procedures were performed in accordance with institutional guidelines at the Friedrich Miescher Institute for Biomedical Research and were approved by the Veterinary Department of the Canton of Basel-Stadt. SOM-ires-Cre (49) and PV-ires-Cre mice (50) were used for Cre-dependent expression of viral vectors. Only heterozygous (Cre/wild type) mice were used for experiments and were backcrossed to a C57BL/6J background for more than ten generations. For all other experiments, male wild-type C57BL/6J mice (Envigo, the Netherlands) were used. Mice were individually housed for at least 14 days before starting behavioral paradigms. Animals were kept in a 12 hours light–dark cycle with access to food and water ad libitum as well as a shelter and a running wheel. All behavioral experiments were conducted during the light cycle.

Surgical procedure

We performed surgeries when mice were 9 to 10 weeks of age. Mice were anesthetized using isoflurane (3 to 5% for induction, 1 to 2% for maintenance; Attane, Provect) in 95% O₂ (Praxair) and fixed in a stereotactic frame (Kopf Instruments). Injections of buprenorphine (Temgesic, Indivior UK Limited; 0.1 mg per kg body weight subcutaneously 30 min before anesthesia) and ropivacain (Naropin, AstraZeneca; 0.1 ml locally under the scalp before incision) were provided for analgesia. Postoperative pain medication included buprenorphine (0.1 mg per kg body weight in the drinking water; overnight) and injections of meloxicam (Metacam, Boehringer Ingelheim; 1 mg per kg body weight subcutaneously) for up to 3 days if necessary. Ophthalmic ointment was applied to avoid eye drying. The body temperature of the experimental animal was maintained at 36°C using a feedback-controlled heating pad (FHC).

For the imaging of somas and dendrites, mice were injected with AAV2/9-CaMKII-Cre-SV40 (2.80.10¹³ GC.ml⁻¹, AV-9-PV2396, UPenn) diluted in sterile saline (final dilution 1:20000) mixed 1:1 with AAV2/1-Syn-Flex-GCaMP6s (51) (1.9.10¹² GC.ml⁻¹, 100845-AAV2/1, Addgene, final dilution: 1:2), resulting in sparse labeling of LA PNs. For combined imaging of LA pyramidal cells and chemogenetic inhibition of SST+ interneurons, SST-ires-Cre mice were injected with an AAV2/1-CaMKII-FLPo diluted in sterile saline (3.4.10¹² GC.ml⁻¹, Vector Biolabs, VB1921, final dilution 1:5000) mixed 1:1:1 with AAV2/1-Efla-fDIO-GCaMP6s (4.2.10¹² GC.ml⁻¹, 105714, Addgene, final dilution 1:3) and AAV2/1-hSyn-DIO-hM4D(Gi)-mCherry (6.4.10¹² GC.ml⁻¹, 44362-AAV2/2, Addgene, final dilution 1:3). For combined imaging of LA pyramidal cells and chemogenetic excitation of SST+ interneurons, SST-ires-Cre mice were injected with an AAV2/1-CaMKII-FLPo diluted in sterile saline (3.4.10¹² GC.ml⁻¹, Vector Biolabs, VB1921, final dilution 1:900) mixed 1:1:1 with AAV2/1-Efla-fDIO-GCaMP6s (4.2.10¹² GC.ml⁻¹, 105714, Addgene, final dilution 1:3) and AAV2/2-hSyn-DIO-hM3D(Gq)-mCherry (7.9.10¹² GC.ml⁻¹, 50474-AAV2/2, Addgene, final dilution 1:3). In the case of control mice, the h3MD(Gq)-mCherry expressing virus was replaced by an equivalent amount of AAV2/2-hSyn-DIO-mCherry (3.9.10¹² GC.ml⁻¹, 50459-AAV2/2, Addgene, final dilution 1:3). The virus mix (300–500 nl) was unilaterally injected into the BLA using a precision micropositioner (Model 2650, Kopf Instruments) and pulled glass pipettes connected to a Picospritzer III microinjection system (Parker Hannifin Corporation) at the following coordinates from bregma: AP: –1.55 mm; ML: –3.4 mm; DV: –3.75 to –4.15 mm. During the same surgery, a GRIN microendoscope (GRIN lens, 0.6 × 7.3 mm, GLP-0673, Inscopix) was implanted into the

LA as previously described (52). In brief, a sterile needle was used to make an incision above the imaging site. The GRIN lens was subsequently lowered into the brain using a micropositioner (coordinates from bregma: AP: –1.55 mm; ML: –3.4 mm; DV: 4.0 mm) with a custom-built lens holder and fixed to the skull using ultraviolet light-curable glue (Henkel, Loctite 4305). A mix of dental acrylic (Paladur, Heraeus) and black acrylic paint was used to seal the skull and attach a custom-made head bar for animal fixation during imaging experiments. Mice were allowed to recover for at least 14 days after GRIN lens implantation before checking for GCaMP expression.

Two-photon imaging

Two to six weeks after surgery, mice were head-fixed on a running wheel to check for sufficient expression of GCaMP6s under a two-photon microscope (Ultima Investigator, Bruker, USA). When sufficient expression level was reached (5 to 10 weeks after surgery), mice were habituated to a brief head-fixation under the microscope for at least 2 consecutive days before any behavioral paradigm, while free to run on a wheel. GCaMP6s signal was recorded at a 30 Hz from a field of view of 471 by 471 μm (512 by 512 pixels) through a water immersion objective [25×, 1.05 numerical aperture (NA), Olympus]. Ultrasound gel (G008, FIAB spA) was used to interface the objective and the GRIN lens. Excitation light was provided with a mode-locked laser system operating at 920 nm, 80-MHz pulse repeat, 120 fs pulse width (Insight X3, Spectra Physics, Mountain View, CA). For simultaneous imaging of GCaMP6s and tdTomato (AAV-CAG-flex-tdTomato, 1.3.10¹³ GC.ml⁻¹, 28306-AAV1, Addgene), excitation light was provided at 960 nm instead and green and red emission light was filtered through specific bandpass filters (green emission light: 525/70 nm; red emission light: 595/50 nm, both Chroma Technology) and detected by different PMTs (photomultipliers, Hamamatsu Photonics). For individual mice, the same imaging parameters were kept across repeated behavioral sessions. Imaging data were recorded using Prairie View Software (Bruker, USA).

For detailed structural scan acquisition and subsequent dendritic arbor reconstruction, mice were hosted for an additional 4 to 6 weeks following any behavioral paradigm to allow for maximal GCaMP6s expression. Then, mice were anesthetized with FMM (Fentanyl-Curamed, 0.05 mg per kg of body weight, Midazolam, 5 mg per kg of body weight, Medetomidine, 0.5 mg per kg of body weight) injected IP (53). Ophthalmic ointment was applied to avoid eye drying. The body temperature of the experimental animal was maintained at 36°C using a feedback-controlled heating

pad (FHC). A 3D imaging volume, centered on the imaging plane previously used for functional imaging, was acquired with a 2 μm increment between each plane. Each image was obtained by averaging 128 frames from a field of view of 471 by 471 μm (1024 by 1024 pixels). The dendritic arbors of the imaged neurons were tracked in 3D using the ImageJ simple neurite tracer plugin (54), projected along the depth dimension and mapped onto the corresponding functional imaging data (fig. S2A). This allowed associating functionally imaged dendritic branches with their parent soma.

Mouse behavior

To assess tone and shock tuning and stability, mice were head-fixed on a running wheel under a 2-photon microscope. A rotary encoder (SparkFun Electronics) was used to record running speed. Mice were allowed to habituate to the setup under head fixation for at least 2 days prior to the start of any experimental paradigm and for at least 15 min prior to the beginning of each experimental session. For auditory stimulus delivery, an electrostatic speaker (ESI, Tucker-Davis Technologies) was placed on each side of the mouse's head. 3 s continuous pure tones (75 to 85 dB, 3 to 18 kHz) were generated using a System 3 RP2.1 real-time processor and a SA1 stereo amplifier with RPDsEx Software (all Tucker-Davis Technologies). Auditory stimuli were presented in a random order of frequencies and with increasing sound pressure levels on 2 consecutive days with an inter-trial interval (ITI) of 90 s. In a subset of mice, the same tone presentation protocol was applied for 4 consecutive days. For electrical shock delivery, a small two pin connector (Fischer Elektronik) was brought in contact to the forehead of the mouse, between the eyes and the ears, and connected to a precision animal shocker delivering direct current (DC). On the last day, 20 to 30 min after the last tone presentation, 1 s electrical shocks with increasing intensities (0.1 to 0.65 mA) were delivered with an inter-trial interval (ITI) of 120 s. Behavioral protocols for stimulus control were generated using the Prairie View Software (Bruker, USA) via TTL (transistor-to-transistor logic) pulses. For chemogenetic reduction of SST+ interneurons synaptic strength, mice were injected IP with saline (0.9% NaCl) on day 1 and with CNO (5 mg per kg, Tocris) on day 2. 1 hour after CNO injection, tones were presented on both days following the same presentation protocol as described in this section.

FC paradigm

Mice were extensively handled and habituated to the head-fixation and electrodes delivering shock for 2-5 days prior to imaging or behavioral recording. On day 1, mice were habituated to a pure tone (CS: 3 s, 7 or 12 kHz; 80 to

85 dB sound pressure level) presented 10 times with a 90 to 120 s inter-trial interval (ITI). On day 2, mice were conditioned to the CS by pairing it with a US (1 s electrical shock, 1 mA) delivered as described in the above section. Alternatively, the US was delivered with two small electrodes brought in contact to the skin of the left forelimb and left hindlimb of the mouse and connected to a precision animal shocker delivering direct current (1 s electrical shock, 1 mA, DC). The US was applied directly after the CS. CSs and USs were each presented 10 times with a 120 s inter-trial interval (ITI). In a separate group of mice that underwent unpaired conditioning, the US was applied at least 120 s apart from any CS. On day 3, similar to day 1, the same pure tones were presented 10 times with a 90 to 120 s inter-trial interval (ITI). For FC paradigm combined with chemogenetic manipulation of interneurons activity, SOM-ires-Cre mice were injected IP with CNO or saline on day 2 and PV-ires-Cre mice on day 3, 30 to 90 min before two-photon imaging.

Freely moving behavior

In parallel with head-fixed FC under a two-photon microscope, fear memory was tested in freely moving conditions in the same animals. On day 1 and 3, mice were placed in a circular arena with Plexiglas walls in a sound-isolated box. After a 2 min baseline period, 3 CSs (30 s, continuous pure tone, 7 or 12 kHz, 80-85 dB sound pressure level) were presented with a 60 to 120 s pseudorandom inter-trial interval (ITI). Freezing responses were quantified on day 1 (habituation) and day 3 (test) during CS presentations. Behavioral protocols for stimulus control were generated using the Radiant software (Plexon) or RPDsEx software (Tucker Davis Technologies) via TTL (transistor-to-transistor logic) pulses. The animal motion was tracked and freezing during the CS presentations on day 1 and day 3 was compared to evaluate associative learning. Due to technical issues during recording, freezing was not measured during day 1 habituation in 3 fear conditioned mice and during day 3 test in one mouse in the unpaired conditioned group. N numbers are indicated in figure legends.

In vitro electrophysiology

Acute brain slice preparation

Mice were deeply anesthetized (ketamine 250 mg per kg and medetomidine 2.5 mg per kg body weight intraperitoneally) and perfused with carbogenated (95% O₂, 5% CO₂) ice-cold slicing solution ([mM] 2.5 KCl, 11 glucose, 234 sucrose, 26 NaHCO₃, 1.25 NaH₂PO₄, 10 MgSO₄, 2 CaCl₂, 340 mOsm). After decapitation, 300 μm coronal BLA slices were prepared in carbogenated ice-cold slicing solution using a vibrating-blade microtome (HM650V, Microm) equipped with a sapphire blade (Dela-

ware Diamond Knives) and allowed to recover for 20 min at 33°C in carbogenated high-osmolarity artificial cerebrospinal fluid (high-Osm aCSF; [mM] 3.2 KCl, 11.8 glucose, 132 NaCl, 27.9 NaHCO₃, 1.34 NaH₂PO₄, 1.07 MgCl₂, 2.14 CaCl₂, 320 mOsm) followed by 40 min incubation at 33°C in carbogenated aCSF ([mM] 3 KCl, 11 glucose, 123 NaCl, 26 NaHCO₃, 1.25 NaH₂PO₄, 1 MgCl₂, 2 CaCl₂, 300 mOsm). Subsequently, slices were kept at RT in carbogenated aCSF until use. The submerged recording chamber was perfused with carbogenated aCSF at a rate of 2 ml · min⁻¹ and maintained at 32°C.

Electrophysiological methods

Whole-cell patch clamp recordings were performed under visual control using an upright microscope (BX50WI, Olympus). Borosilicate glass pipettes (Harvard Apparatus 30-0068 Glass Capillaries GC150TF-7.5, 1.5 OD × 1.17 ID × 75 L mm) with resistances ranging from 3 to 7 megohms were pulled using a DMZ Universal electrode puller. Pipettes were filled using an intracellular solution allowing for EPSC and IPSC recording [(mM) 120 Cs-gluconate, 11 CsCl, 1 MgCl₂, 1 CaCl₂, 10 HEPES, 11 EGTA, 5 QX-314; 280 mOsm × kg⁻¹; pH adjusted to 7.3 with CsOH]. mCherry+ interneurons were visualized using epifluorescence and a 40× water immersion objective (LumPlanFl 40×/0.8, Olympus). Whole-cell patch clamp recordings were obtained from mCherry- putative principal LA/BLA neurons in regions showing robust somatic DREADD-mCherry expression. During voltage-clamp experiments neurons were held at 0 mV to measure IPSCs. Whole-cell voltage clamp recordings were performed using a MultiClamp 700B amplifier, filtered at 8 kHz and digitized at 20 kHz using a Digidata 1440A digitizer (Molecular Devices).

Electrophysiology data analysis

Data was analyzed using the Python package pyABF (<https://sw Harden.com/pyabf>). For line plots electrical stimulation responses were averaged in a 30 s sliding window. For quantification, responses 1.5 min to 0 min before CNO application were compared to responses 0.5 to 2.5 min after CNO application as indicated by the shaded area of the line plots to allow for CNO diffusion throughout the brain slice.

Calcium imaging data extraction

Basic image pre-processing: briefly, for each imaging session, recordings from all trials were concatenated into an image stack, corrected for bidirectional scanning (55), down sampled spatially by 2 by 2 pixels. Residual background was calculated with a disk-shaped morphological structuring element 'strel' in Matlab (MathWorks) and subtracted from the

signal. Then, images were corrected for rigid and for non-rigid motion using Normcor (55). Registration across imaging sessions: after pre-processing as described, the mean intensity projections of each imaging session were registered using imregister in Matlab (MathWorks) and the resulting shifts applied to single frames. To check that GCaMP signal alone is sufficient for appropriate motion registration of subcellular compartments, we conducted a control experiment to compare image registration using either GCaMP or the fluorescence-independent fluorescent marker tdtomato as reference (fig. S2, H to M). For selecting subcellular compartments, non-overlapping somas, dendritic branches and dendritic spines were selected manually as regions of interest (ROIs) in ImageJ using the ROI manager tool (polygon selection for somas, line selection with 3 pixels \approx 2 μ m width for dendrites, oval selection with 4 to 7 pixels \approx 3 to 5 μ m for dendritic spines to account for small difference between imaging sessions) and carefully inspected for the absence of overlap with other subcellular compartments. The mean fluorescence intensity of all pixels from each ROI was considered for further analysis. Relative changes in Ca^{2+} fluorescence (F) were calculated using the formula: $\Delta F/F_0 = (F - F_0)/F_0$ (with $F_0 = 33$ rd percentile of the fluorescence intensity over the entire trace) and used for all analysis of Ca^{2+} activity.

Data analysis

To identify responsive subcellular compartments, average Ca^{2+} traces were compared between the stimulus presentation period and a baseline period of the same duration. The stimulus response period was set to 1 s for shock presentations. For FC, US responsiveness was assessed by using the last second of CS presentation as baseline instead. Somas and dendrites with a CS offset response during the habituation day were not considered US responsive. If the mean Ca^{2+} activity during the stimulus period was larger or smaller than the mean Ca^{2+} activity during the baseline period by more than 2 SD (standard deviations), the ROI was classified as responsive (excited or inhibited, depending on response sign). Otherwise, the ROI was classified as non-responsive. To identify functional subclasses of neurons, we classified neurons in four mutually exclusive categories based on their CS responses on day 1 (habituation) and day 3 (test) as follows: (i) CS non-responsive: CS non-responsive on day 1 and day 3; (ii) CS neutral: same CS response sign (positive or negative response) on day 1 and on day 3 and absolute difference between the CS responses on day 1 and day 3 smaller than 15% $\Delta F/F_0$; (iii) CSup: CS response on day 3 larger than on day 1, excluding CS non-responsive and CS neutral neurons; (iv) CSdown: CS response on

day 3 smaller than on day 1, excluding CS non-responsive and CS neutral neurons. For intra-session CS response amplitude comparison, responses to the first and the last CS presentation on each session were compared. One-term Gaussian models were used to fit histogram distributions following the equation: $f(x) = a1 \cdot \exp\{-(x - b1)/c1\}^2$. All analysis was conducted in Matlab.

Probability and amplitude of stimulus response

To assess response probability, Ca^{2+} activity was compared between the stimulus presentation period and a baseline period of the same duration. The stimulus response period was set to 3 s for shock presentations. Response probability was defined as the proportion of trials where the mean Ca^{2+} activity during the stimulus period was larger than 2 SD (standard deviations) of the Ca^{2+} activity during the baseline period. Response amplitude was calculated from the average of all responsive trials. To compare the probability of response between days, the ratio of response probability was computed for each compartment. To compare the amplitude of response between days, the difference of response amplitude was computed for each compartment.

Calcium transient detection and normalization

Ca^{2+} transients were detected in somas, dendritic branches and dendritic spines using the findpeaks Matlab function with the following criteria: $\Delta F/F_0$ exceeding 1 SD (standard deviation) of the entire trace, prominence exceeding 0.5 SD (standard deviation) of the entire trace. This method reduces the influence of differences in signal-to-noise ratio when comparing Ca^{2+} activity between compartments (fig. S2). The same method was used to detect negative transients from the negative $\Delta F/F_0$ trace ($-\Delta F/F_0$) in order to estimate the rate of false-positive events (56). Within single neurons, Ca^{2+} transients in the dendrites and soma were defined as co-occurring when their peak amplitude was detected within a time window of 1 s in order to account for the variability of the Ca^{2+} indicator rise time in different compartments. Events were classified as compartment-specific (e.g., dendrite only) or co-occurring (e.g., soma + dendrite) relative to the dendrites or spines. For example, if co-occurring transients were detected in dendrite 1 and in its parent soma and undetected in dendrite 2, this transient was classified as soma + dendrite in dendrite 1 but not in dendrite 2).

Ca^{2+} transients detected during the tone presentation period were defined as tone-locked, Ca^{2+} transients detected outside of the tone presentation period as spontaneous. To compare the amplitude of Ca^{2+} transients in the soma and in dendritic branches, the Ca^{2+} trace of each compartment was normalized to

its maximum $\Delta F/F_0$ over the course of all concatenated sessions. Correlation between somatic and dendritic Ca^{2+} activity was measured using the Pearson's correlation coefficient (r) of the normalized Ca^{2+} signal time course over the considered time period (57). Event amplitude correlation was measured with the Pearson's correlation coefficient (r) of the somatic and dendritic normalized amplitude of the automatically detected transients over the course of the entire considered session (5 transients minimum per session). Each session consists of concatenated stimuli presentations (30 s each, including 10 s pre-stimulus baseline). For spontaneous calcium events $\Delta F/F_0$ integral calculation and for comparison of spontaneous versus CS-locked $\Delta F/F_0$ integral, the area under the full width at half maximum of the automatically detected peak was considered. For calculation of CS-locked $\Delta F/F_0$ integral, the area under the curve during the tone presentation window (3 s) was considered.

Histology and fluorescent immunohistochemistry

Following completion of any behavioral paradigm and structural scans, mice were transcardially perfused. Mice were anesthetized with an intraperitoneal injection of an anesthetic mixture (250 mg/kg ketamine and 2.5 mg/kg medetomidine) to achieve deep anesthesia. The mice were then perfused transcardially with 0.1 M phosphate-buffered saline (PBS, pH 7.4) for 2 min followed by 4% paraformaldehyde (PFA) in PBS for 10–40 min. Then, the brains were removed from the skull and further incubated in 4% PFA for 2–4 hours at 4°C, then cut into 100 μ m coronal slices using a vibratome (VT1000S). Perfusion-fixed sections containing the amygdala were dried on slides and covered with Aqua-Poly/Mount (Polysciences). Sections were scanned with a laser scanning confocal microscope (LSM700) equipped with a 10 \times air objective (Plan-Apochromat 10 \times /0.45) or with a Zeiss Axio Scan Z1 Slide scanner equipped with a Zeiss objective (Fluar 5 \times /0.25) to confirm DREADD-mCherry expression and GRIN lens implantation site. GRIN lens placements were matched against a mouse brain atlas (fig. S1A) (58).

Statistical analyses and data presentation

Statistical analyses were carried out using Matlab (MathWorks). The sample sizes are similar to those used in the field. No statistical methods were used to determine sample size. Littermates were randomly allocated to experimental groups without pre-determined criteria and could be later identified by unique markers for group assignment. Experimenters were not blind to the group assignment of the animals. Animals were post hoc excluded from the analysis in the following three cases: (i) the

bottom tip of the GRIN lens was located outside the LA; (ii) brain motion was too great to be corrected post-hoc; (3) GCaMP6 labeling was not sparse enough to allow isolation of dendritic signals. The following number of mice were rejected, given for each per cohort: sensory stimuli tuning and stability: $n = 1$ mouse; FC: $n = 4$ mice; Unpaired conditioning: $n = 3$ mice, SST+ hM3D: $n = 4$ mice, SST+ mCherry: $n = 2$ mice, PV+ hM4D: $n = 3$ mice. The number of data points from separate cells and/or animal are indicated in figures, legends and supplementary tables. Averaging across multiple trials per cell/animal is indicated where applicable and n numbers always refer to data from individual cells/animals. Results described throughout the paper were reproduced. Multiple rounds of experimentation were required, i.e., from multiple mice, which were averaged for the presented datasets. Data was acquired from mice from multiple litters, and responses from individual cells were collected from at least four mice per group. All datasets were tested for normal distribution using a Shapiro-Wilk normality test. If the null hypothesis of normal distribution was not rejected, datasets were compared using a Student's t test or unpaired Student's t test, as appropriate. The corresponding one-sample tests were used to compare datasets to a fixed value. One-way analysis of variance (ANOVA) or Kruskal-Wallis tests were used when comparing more than two datasets, as appropriate. Post hoc multiple comparisons were performed using the Bonferroni correction. If the null hypothesis of normal distribution was rejected, datasets were compared using Wilcoxon signed-rank test or a Wilcoxon signed-rank test, as appropriate. The corresponding one-sample tests were used to compare datasets to a fixed value. A Fisher's exact test was conducted to compare proportions between two groups. Box-and-whisker plots show median values and 25th and 75th percentiles, the maximum whiskers length is 1.5 times the interquartile range. The corresponding mean \pm SEM values for each test is reported in Table S1. A statistical significance threshold was set at 0.05, and significance levels are presented as $*P < 0.05$, $**P < 0.01$ or $***P < 0.001$ in all figures. Averaging across multiple trials is indicated in the figure legends and respective methods sections where applicable. Contrast and brightness of representative example images were minimally adjusted using ImageJ or Zen lite Software (ZEISS technology). For figure display, Ca^{2+} traces were presented as $\Delta F/F_0$ or z-score ($z = (F - F_0) / \sigma$, with F_0 = mean fluorescence and σ = standard deviation over the entire Ca^{2+} traces).

REFERENCES AND NOTES

- M. London, M. Häusser, Dendritic computation. *Annu. Rev. Neurosci.* **28**, 503–532 (2005). doi: [10.1146/annurev.neuro.28.061604.135703](https://doi.org/10.1146/annurev.neuro.28.061604.135703); pmid: [16033324](https://pubmed.ncbi.nlm.nih.gov/16033324/)
- G. Major, M. E. Larkum, J. Schiller, Active properties of neocortical pyramidal neuron dendrites. *Annu. Rev. Neurosci.* **36**, 1–24 (2013). doi: [10.1146/annurev-neuro-062111-150343](https://doi.org/10.1146/annurev-neuro-062111-150343); pmid: [23841837](https://pubmed.ncbi.nlm.nih.gov/23841837/)
- N.-L. Xu et al., Nonlinear dendritic integration of sensory and motor input during an active sensing task. *Nature* **492**, 247–251 (2012). doi: [10.1038/nature11601](https://doi.org/10.1038/nature11601); pmid: [23143335](https://pubmed.ncbi.nlm.nih.gov/23143335/)
- N. Takahashi, T. G. Oertner, P. Hegemann, M. E. Larkum, Active cortical dendrites modulate perception. *Science* **354**, 1587–1590 (2016). doi: [10.1126/science.1246066](https://doi.org/10.1126/science.1246066); pmid: [28008068](https://pubmed.ncbi.nlm.nih.gov/28008068/)
- J. Voigts, M. T. Harnett, Somatic and dendritic encoding of spatial variables in retrosplenial cortex differs during 2D navigation. *Neuron* **105**, 237–245.e4 (2020). doi: [10.1016/j.neuron.2019.10.016](https://doi.org/10.1016/j.neuron.2019.10.016); pmid: [31759808](https://pubmed.ncbi.nlm.nih.gov/31759808/)
- J. Cichon, W. B. Gan, Branch-specific dendritic Ca^{2+} spikes cause persistent synaptic plasticity. *Nature* **520**, 180–185 (2015). doi: [10.1038/nature14251](https://doi.org/10.1038/nature14251); pmid: [25822789](https://pubmed.ncbi.nlm.nih.gov/25822789/)
- M. E. J. Sheffield, D. A. Dombeck, Calcium transient prevalence across the dendritic arbour predicts place field properties. *Nature* **517**, 200–204 (2015). doi: [10.1038/nature13871](https://doi.org/10.1038/nature13871); pmid: [25363782](https://pubmed.ncbi.nlm.nih.gov/25363782/)
- A. Losonczy, J. K. Makara, J. C. Magee, Compartmentalized dendritic plasticity and input feature storage in neurons. *Nature* **452**, 436–441 (2008). doi: [10.1038/nature06725](https://doi.org/10.1038/nature06725); pmid: [18368112](https://pubmed.ncbi.nlm.nih.gov/18368112/)
- G. Schoenfeld et al., Dendritic integration of sensory and reward information facilitates learning. *bioRxiv* 474360 [Preprint] (2022). doi: [10.1101/2021.12.28.474360](https://doi.org/10.1101/2021.12.28.474360)
- L. Beaulieu-Laroche, E. H. S. Toloza, N. J. Brown, M. T. Harnett, Widespread and highly correlated somato-dendritic activity in cortical layer 5 neurons. *Neuron* **103**, 235–241.e4 (2019). doi: [10.1016/j.neuron.2019.05.014](https://doi.org/10.1016/j.neuron.2019.05.014); pmid: [31178115](https://pubmed.ncbi.nlm.nih.gov/31178115/)
- A. Kerlin et al., Functional clustering of dendritic activity during decision-making. *eLife* **8**, e46966 (2019). doi: [10.7554/eLife.46966](https://doi.org/10.7554/eLife.46966); pmid: [31663507](https://pubmed.ncbi.nlm.nih.gov/31663507/)
- V. Francioni, Z. Padamsey, N. L. Rochefort, High and asymmetric somato-dendritic coupling of V1 layer 5 neurons independent of visual stimulation and locomotion. *eLife* **8**, e49145 (2019). doi: [10.7554/eLife.49145](https://doi.org/10.7554/eLife.49145); pmid: [31880536](https://pubmed.ncbi.nlm.nih.gov/31880536/)
- M. S. Fanselow, A. M. Poulos, The neuroscience of mammalian associative learning. *Annu. Rev. Psychol.* **56**, 207–234 (2005). doi: [10.1146/annurev.psych.56.091103.070213](https://doi.org/10.1146/annurev.psych.56.091103.070213); pmid: [15709934](https://pubmed.ncbi.nlm.nih.gov/15709934/)
- H. T. Blair, G. E. Schafe, E. P. Bauer, S. M. Rodrigues, J. E. LeDoux, Synaptic plasticity in the lateral amygdala: A cellular hypothesis of fear conditioning. *Learn. Mem.* **8**, 229–242 (2001). doi: [10.1101/lm.30901](https://doi.org/10.1101/lm.30901); pmid: [11584069](https://pubmed.ncbi.nlm.nih.gov/11584069/)
- C. W. Butler et al., Neurons specifically activated by fear learning in lateral amygdala display increased synaptic strength. *eNeuro* **5**, 114 (2018). doi: [10.1523/ENEURO.0114-18.2018](https://doi.org/10.1523/ENEURO.0114-18.2018); pmid: [30027112](https://pubmed.ncbi.nlm.nih.gov/30027112/)
- S. Maren, Neurobiology of Pavlovian fear conditioning. *Annu. Rev. Neurosci.* **24**, 897–931 (2001). doi: [10.1146/annurev.neuro.24.1.897](https://doi.org/10.1146/annurev.neuro.24.1.897); pmid: [11520922](https://pubmed.ncbi.nlm.nih.gov/11520922/)
- M. T. Rogan, U. V. Staubli, J. E. LeDoux, Fear conditioning induces associative long-term potentiation in the amygdala. *Nature* **390**, 604–607 (1997). doi: [10.1038/37601](https://doi.org/10.1038/37601); pmid: [9403688](https://pubmed.ncbi.nlm.nih.gov/9403688/)
- M. Bocchio, S. Nabavi, M. Capogna, Synaptic Plasticity, Engrams, and Network Oscillations in Amygdala Circuits for Storage and Retrieval of Emotional Memories. *Neuron* **94**, 731–743 (2017). doi: [10.1016/j.neuron.2017.03.022](https://doi.org/10.1016/j.neuron.2017.03.022); pmid: [28521127](https://pubmed.ncbi.nlm.nih.gov/28521127/)
- X. Zhang, B. Li, *Nat. Commun.* **9**, 1 (2018). doi: [10.1038/s41467-017-02088-w](https://doi.org/10.1038/s41467-017-02088-w); pmid: [29317637](https://pubmed.ncbi.nlm.nih.gov/29317637/)
- J. Gründemann et al., Amygdala ensembles encode behavioral states. *Science* **364**, eaav8736 (2019). doi: [10.1126/science.aav8736](https://doi.org/10.1126/science.aav8736); pmid: [31000636](https://pubmed.ncbi.nlm.nih.gov/31000636/)
- B. F. Grewe et al., Neural ensemble dynamics underlying a long-term associative memory. *Nature* **543**, 670–675 (2017). doi: [10.1038/nature21682](https://doi.org/10.1038/nature21682); pmid: [28329757](https://pubmed.ncbi.nlm.nih.gov/28329757/)
- J. P. Johansen, C. K. Cain, L. E. Ostroff, J. E. LeDoux, Molecular mechanisms of fear learning and memory. *Cell* **147**, 509–524 (2011). doi: [10.1016/j.cell.2011.10.009](https://doi.org/10.1016/j.cell.2011.10.009); pmid: [22036561](https://pubmed.ncbi.nlm.nih.gov/22036561/)
- S. Krabbe et al., Adaptive disinhibitory gating by VIP interneurons permits associative learning. *Nat. Neurosci.* **22**, 1834–1843 (2019). doi: [10.1038/s41593-019-0508-y](https://doi.org/10.1038/s41593-019-0508-y); pmid: [31636447](https://pubmed.ncbi.nlm.nih.gov/31636447/)
- S. B. E. Wolff et al., Amygdala interneuron subtypes control fear learning through disinhibition. *Nature* **509**, 453–458 (2014). doi: [10.1038/nature13258](https://doi.org/10.1038/nature13258); pmid: [24814341](https://pubmed.ncbi.nlm.nih.gov/24814341/)
- C. Q. Chiu et al., Compartmentalization of GABAergic inhibition by dendritic spines. *Science* **340**, 759–762 (2013). doi: [10.1126/science.1234274](https://doi.org/10.1126/science.1234274); pmid: [23661763](https://pubmed.ncbi.nlm.nih.gov/23661763/)
- Y. Kasugai et al., Structural and functional remodeling of amygdala GABAergic synapses in associative fear learning. *Neuron* **104**, 781–794.e4 (2019). doi: [10.1016/j.neuron.2019.08.013](https://doi.org/10.1016/j.neuron.2019.08.013); pmid: [31543297](https://pubmed.ncbi.nlm.nih.gov/31543297/)
- Y. Humeau et al., Dendritic spine heterogeneity determines afferent-specific Hebbian plasticity in the amygdala. *Neuron* **45**, 119–131 (2005). doi: [10.1016/j.neuron.2004.12.019](https://doi.org/10.1016/j.neuron.2004.12.019); pmid: [15629707](https://pubmed.ncbi.nlm.nih.gov/15629707/)
- S. Krabbe, J. Gründemann, A. Lüthi, Amygdala inhibitory circuits regulate associative fear conditioning. *Biol. Psychiatry* **83**, 800–809 (2018). doi: [10.1016/j.biopsych.2017.10.006](https://doi.org/10.1016/j.biopsych.2017.10.006); pmid: [29174478](https://pubmed.ncbi.nlm.nih.gov/29174478/)
- J. J. Letzkus et al., A disinhibitory microcircuit for associative fear learning in the auditory cortex. *Nature* **480**, 331–335 (2011). doi: [10.1038/nature10674](https://doi.org/10.1038/nature10674); pmid: [22158104](https://pubmed.ncbi.nlm.nih.gov/22158104/)
- E. Abs et al., Learning-related plasticity in dendrite-targeting layer 1 interneurons. *Neuron* **100**, 684–699.e6 (2018). doi: [10.1016/j.neuron.2018.09.001](https://doi.org/10.1016/j.neuron.2018.09.001); pmid: [30269988](https://pubmed.ncbi.nlm.nih.gov/30269988/)
- G. Kastellakis, P. Poirazi, Synaptic clustering and memory formation. *Front. Mol. Neurosci.* **12**, 300 (2019). doi: [10.3389/fnmol.2019.00300](https://doi.org/10.3389/fnmol.2019.00300); pmid: [31866824](https://pubmed.ncbi.nlm.nih.gov/31866824/)
- M. Häusser, B. Mel, Dendrites: Bug or feature? *Curr. Opin. Neurobiol.* **13**, 372–383 (2003). doi: [10.1016/S0959-4388\(03\)00075-8](https://doi.org/10.1016/S0959-4388(03)00075-8); pmid: [12850223](https://pubmed.ncbi.nlm.nih.gov/12850223/)
- G. Kastellakis, A. J. Silva, P. Poirazi, Linking memories across time via neuronal and dendritic overlaps in model neurons with active dendrites. *Cell Rep.* **17**, 1491–1504 (2016). doi: [10.1016/j.celrep.2016.10.015](https://doi.org/10.1016/j.celrep.2016.10.015); pmid: [27806290](https://pubmed.ncbi.nlm.nih.gov/27806290/)
- J. H. Choi et al., Interregional synaptic maps among engrain cells underlie memory formation. *Science* **360**, 430–435 (2018). doi: [10.1126/science.aas9204](https://doi.org/10.1126/science.aas9204); pmid: [29700265](https://pubmed.ncbi.nlm.nih.gov/29700265/)
- D. W. Bloodgood, J. A. Sugam, A. Holmes, T. L. Kash, Fear extinction requires infralimbic cortex projections to the basolateral amygdala. *Transl. Psychiatry* **8**, 60 (2018). doi: [10.1038/s41398-018-0106-x](https://doi.org/10.1038/s41398-018-0106-x); pmid: [29507292](https://pubmed.ncbi.nlm.nih.gov/29507292/)
- H. Motani, M. Maroun, E. Barkai, Learning-induced bidirectional plasticity of intrinsic neuronal excitability reflects the valence of the outcome. *Cereb. Cortex* **24**, 1075–1087 (2014). doi: [10.1093/cercor/bhs394](https://doi.org/10.1093/cercor/bhs394); pmid: [23236201](https://pubmed.ncbi.nlm.nih.gov/23236201/)
- M. Sehgal, V. L. Ehlers, J. R. Moyer Jr., Learning enhances intrinsic excitability in a subset of lateral amygdala neurons. *Learn. Mem.* **21**, 161–170 (2014). doi: [10.1101/lm.032730.113](https://doi.org/10.1101/lm.032730.113); pmid: [24554670](https://pubmed.ncbi.nlm.nih.gov/24554670/)
- E. K. Lucas, A. M. Jegaraj, H. Morishita, R. L. Clem, Multimodal and site-specific plasticity of amygdala parvalbumin interneurons after fear learning. *Neuron* **91**, 629–643 (2016). doi: [10.1016/j.neuron.2016.06.032](https://doi.org/10.1016/j.neuron.2016.06.032); pmid: [27427462](https://pubmed.ncbi.nlm.nih.gov/27427462/)
- R. D. Samson, É. C. Dumont, D. Paré, Feedback inhibition defines transverse processing modules in the lateral amygdala. *J. Neurosci.* **23**, 1966–1973 (2003). doi: [10.1523/JNEUROSCI.23-05-01966.2003](https://doi.org/10.1523/JNEUROSCI.23-05-01966.2003); pmid: [12629202](https://pubmed.ncbi.nlm.nih.gov/12629202/)
- P. Botta et al., Regulating anxiety with extrasynaptic inhibition. *Nat. Neurosci.* **18**, 1493–1500 (2015). doi: [10.1038/nn.4102](https://doi.org/10.1038/nn.4102); pmid: [26322928](https://pubmed.ncbi.nlm.nih.gov/26322928/)
- A. G. Khan et al., Distinct learning-induced changes in stimulus selectivity and interactions of GABAergic interneuron classes in visual cortex. *Nat. Neurosci.* **21**, 851–859 (2018). doi: [10.1038/s41593-018-0143-z](https://doi.org/10.1038/s41593-018-0143-z); pmid: [29786081](https://pubmed.ncbi.nlm.nih.gov/29786081/)
- D. E. Wilson, B. Scholl, D. Fitzpatrick, Differential tuning of excitation and inhibition shapes direction selectivity in ferret visual cortex. *Nature* **560**, 97–101 (2018). doi: [10.1038/s41586-018-0354-1](https://doi.org/10.1038/s41586-018-0354-1); pmid: [30046106](https://pubmed.ncbi.nlm.nih.gov/30046106/)
- F. Zenke, W. Gerstner, S. Ganguli, The temporal paradox of Hebbian learning and homeostatic plasticity. *Curr. Opin. Neurobiol.* **43**, 166–176 (2017). doi: [10.1016/j.conb.2017.03.015](https://doi.org/10.1016/j.conb.2017.03.015); pmid: [28431369](https://pubmed.ncbi.nlm.nih.gov/28431369/)
- K. A. Wilmes, H. Sprekeler, S. Schreiber, Inhibition as a binary switch for excitatory plasticity in pyramidal neurons. *PLOS Comput. Biol.* **12**, e1004768 (2016). doi: [10.1371/journal.pcbi.1004768](https://doi.org/10.1371/journal.pcbi.1004768); pmid: [27003565](https://pubmed.ncbi.nlm.nih.gov/27003565/)
- A. P. Yiu et al., Neurons are recruited to a memory trace based on relative neuronal excitability immediately before training. *Neuron* **83**, 722–735 (2014). doi: [10.1016/j.neuron.2014.07.017](https://doi.org/10.1016/j.neuron.2014.07.017); pmid: [25102562](https://pubmed.ncbi.nlm.nih.gov/25102562/)
- P. Namburi et al., A circuit mechanism for differentiating positive and negative associations. *Nature* **520**, 675–678 (2015). doi: [10.1038/nature14366](https://doi.org/10.1038/nature14366); pmid: [25925480](https://pubmed.ncbi.nlm.nih.gov/25925480/)
- A. Beyeler et al., Organization of valence-encoding and projection-defined neurons in the basolateral amygdala. *Cell Rep.* **22**, 905–918 (2018). doi: [10.1016/j.celrep.2017.12.097](https://doi.org/10.1016/j.celrep.2017.12.097); pmid: [29386133](https://pubmed.ncbi.nlm.nih.gov/29386133/)

48. P. Poirazi, A. Papoutsi, Illuminating dendritic function with computational models. *Nat. Rev. Neurosci.* **21**, 303–321 (2020). doi: [10.1038/s41583-020-0301-7](https://doi.org/10.1038/s41583-020-0301-7); pmid: [32393820](https://pubmed.ncbi.nlm.nih.gov/32393820/)

ACKNOWLEDGMENTS

We thank all members of the Lüthi group for helpful discussions and comments on the work; G. Keller, D. Gerosa Erni, and T. Lu for virus production; P. Argast, C. Mueller, T. Eichlisberger, and all staff of the FMI Animal Facility for excellent technical assistance; J. Eglinger, S. Bourke, and R. Thierry at the FMI imaging facility and the FMI IT department for their dedicated technical support; and V. Jayaraman, R. Kerr, D. Kim, L. Looger, K. Svoboda, and the HHMI Janelia GENIE Project for making GCaMP6 available. **Funding:** This work was supported by the Novartis Research Foundation, the European Research Council (ERC) under the European Union's Horizon 2020 Research and Innovation Programme (grant agreements 669582 to A.L. and 803870 to J.G.), the National Center

of Competences in Research: “SYNAPSY—The Synaptic Bases of Mental Diseases” (financed by the Swiss National Science Foundation SNSF, 51NF40-158776), SNSF core (310030B_170268; all to A.L.), and SNSF Professorship (PP00P3_170672 to J.G) grants; as well as a Young Investigator Grant from the Brain & Behavior Research Foundation (23593), a Career Development Award from the Synapsis Foundation—Alzheimer Research Switzerland ARS (2018-CDA02), and the Fondazione HED ALBIREO (to S.K.). A.S. was supported by a postdoctoral fellowship from the European Molecular Biology Organization (EMBO-ALTF-233-2020). **Author contributions:** S.D., S.K., J.G., and A.L. designed the project. S.D. and A.S. performed imaging experiments. S.D. performed imaging data analysis. M.M. performed in vitro patch-clamp experiments. S.D. and S.K. designed, generated, and tested the viral constructs. All authors contributed to the experimental design and interpretation of the data and wrote the manuscript. **Competing interests:** The authors declare no competing interests. **Data and materials availability:** All data and analyses necessary to understand and assess the conclusions of

the manuscript are presented in the main text and in the supplementary materials. All processed data and scripts needed to evaluate the conclusions in the paper are available at <https://data.fmi.ch/PublicationSupplementRepo> with no access restriction.

SUPPLEMENTARY MATERIALS

science.org/doi/10.1126/science.abf7052

Figs. S1 to S11

Tables S1 and S2

References (49–58)

MDAR Reproducibility Checklist

Movies S1 and S2

[View/request a protocol for this paper from Bio-protocol.](#)

13 November 2020; resubmitted 6 January 2022

Accepted 10 March 2022

10.1126/science.abf7052